

Effective inertia spring tensor model for acoustic materials with coupled local resonancesKenny L. S. Yip^{✉*} and Sajeew John[†]*Department of Physics, University of Toronto, 60 St. George Street, Toronto, Ontario, Canada M5S 1A7*

(Received 8 June 2021; accepted 3 August 2021; published 16 August 2021)

We present a simple physical picture and precise model for the low-frequency acoustic modes of phononic crystals with multiple local resonances within each unit cell and their coupling to spatially separated resonators. The physical picture is a generalization of the widely quoted mass-in-a-box representation of resonant acoustic metamaterials. Our model consists of an array of frequency-dependent effective masses and moments of inertia coupled to near and distant neighbors by a wave-vector-dependent effective spring constant matrix. We demonstrate, using several two-dimensional models, that our simple representation accurately recaptures exact phononic band structure involving coupled translational and rotational modes. Our simplified but precise description is ideally suited for resonators consisting of multiple rigid cores and shells embedded in a softer elastic background. This enables a rich spectrum of acoustic modes and band gaps at audible frequencies, using millimeter to centimeter scale resonators. Our model is readily generalized to three-dimensional phononic crystals. It is suggested that suitable modifications of the spring tensor may enable description of disordered resonant acoustic media.

DOI: [10.1103/PhysRevB.104.054302](https://doi.org/10.1103/PhysRevB.104.054302)**I. INTRODUCTION**

Early theoretical and experimental work on phononic crystals centered around the existence of phononic band gaps in periodic arrays of elastic materials [1–4]. For the structure to exhibit phononic crystal functionality at audible frequencies, the characteristic length scale of the structures must be comparable to the acoustic wavelength. In nonresonant structures, this requires impractically large feature sizes. For example, the wavelength of the A440 tuning pitch is of the order of 1 m in air and 10 m in stiff solids. Conventional nonresonant phononic crystals would require excessively large unit cells to provide band gaps or flat bands at this wavelength. Liu *et al.* proposed a locally resonant sonic material, with a lattice constant of 1.55 cm, exhibiting a subwavelength acoustic band gap in the audible range from 400 to 600 Hz [5]. The structure consisted of dense, stiff lead spheres encapsulated by light, elastic silicone rubber. Further studies confirmed the existence of resonance-based band gaps when the coating material is soft compared to the core and the background [6]. Locally resonant acoustic materials have opened up possibilities of real-world applications from acoustic absorbers and signal filters to acoustic cloaking [7], as well as sub-diffraction-limit lensing [8].

Previously, an elastostatic analysis was applied to individual local resonators to derive analytical expressions for effective, frequency-dependent mass densities [9]. The treatment relied on the small size of the resonators compared to the wavelength, so that wavelike deformation within each

resonator could be ignored. In two-dimensional structures with translational invariance in the axial direction, a resonator encapsulated by a rigid shell has four degrees of freedom that couple to the background, namely, out-of-plane translation, in-plane translations in two orthogonal directions, and in-plane rotation. An effective mass density was determined for each type of resonance. These frequency-dependent mass densities were individually applied to calculate the acoustic band structure using the cutting surface method (CSM) [9,10]. In this effective medium model, the region of the resonators was replaced by a hypothetical medium of uniform, but frequency-dependent effective density. While this approach recaptured the low-frequency, out-of-plane acoustic bands in a two-dimensional structure, it failed to recapture vibrational modes involving the intricate coupling between the different types of resonances of the in-plane acoustic modes. A more fundamental physical picture than the widely used mass-in-a-box representation of individual local resonances [11] is required to describe the nonlocal couplings between resonances.

In this paper, we introduce an effective inertia spring tensor (EIST) model that properly treats the coupling between the in-plane translational and rotational resonances. In addition to replacing the resonator by a hypothetical set of frequency-dependent, uniform density materials, our model incorporates wave-vector-dependent forces and torques acting on the resonators by the elastic background. The frequency-dependent, effective masses and moments of inertia are acted upon by these forces and torques through a generalized expression of Newton's second law. Essentially, the frequency-dependent inertia recaptures internal oscillations of the resonators, whereas the wave-vector-dependent spring tensor describes the external forces due to the displacements from equilibrium of all other units in the phononic crystal. The resultant

* Author to whom correspondence should be addressed: lkyip@physics.utoronto.ca

[†] john@physics.utoronto.ca

acoustic mode spectrum is described by a quadratic equation for the out-of-plane modes, and a higher-order polynomial equation, defined by a 3×3 matrix eigenvalue equation, for the in-plane modes. In contrast to previous literature, our EIST model simultaneously incorporates the effective masses and moments of inertia describing multiple internal degrees of freedom. An external spring tensor allows appropriate coupling of one type of resonance at an oscillator with a different type of resonance at a neighboring oscillator. This provides a transparent and precise physical picture for all the low-frequency acoustic modes. We apply the EIST model to obtain nearly exact low-frequency acoustic band structures of (A) a conventional, nonresonant elastic composite, (B) a locally resonant phononic crystal with one resonance for each degree of freedom, and (C) a locally resonant phononic crystal with multiple resonances for each degree of freedom. In the last example with multiple resonances, we demonstrate, using a lattice constant of 1 cm, two disjoint band gaps $343 \text{ Hz} < f < 487 \text{ Hz}$, and $585 \text{ Hz} < f < 878 \text{ Hz}$ for the in-plane modes over the audible frequency range. The nine low-frequency in-plane acoustic bands are accurately recaptured by our EIST model within 4.0% error, compared to the exact finite-element method (FEM) results of the original phononic crystal. This demonstrates the efficacy of our EIST model in designing locally resonant acoustic structures for sound manipulations. It also suggests possible representations of certain disordered media, via a modified spring tensor (partially) averaged over a range of orientations of the wave vector.

Our EIST approach is distinct from the existing homogenization and effective medium approaches in the literature. In conventional homogenization approaches, the entire structure is approximated as an effective medium [12–15], and the effective parameters are often empirically defined using the transmission spectrum [5] or the acoustic band structure [13,16]. Another effective medium approach is the coherent potential approximation that compares the partial waves from the resonant scatterer and a nonresonant isotropic replacement medium in the long-wavelength limit [16,17]. In our EIST model, the resonators are represented by the effective inertia and the elastic background is described by a spring tensor. The effective masses and moments of inertia are analytically derived using elastostatic analysis, and are expressible as closed-form rational functions of frequency squared.

This paper is organized as follows. In Sec. II, we introduce the effective inertia spring tensor (EIST) model to describe the mode spectrum of a lattice of acoustic resonators with rigid shells embedded in a soft elastic background. In Sec. III, we apply our EIST model to a periodic array of rigid cylinders and obtain the spring tensor suitable for all structures considered in this paper. In Sec. IV, we apply our EIST model to a lattice of locally resonant cylinders with one resonance in each degree of freedom. In Sec. V, we apply our EIST model to a more complex system with multiple, coupled, local resonances. In all three illustrations, we compare the results of the EIST model with the exact acoustic band structure obtained by the finite-element method. In Sec. VI, we discuss the possible extensions of our EIST model to three-dimensional systems and weakly disordered phononic crystals. In Appendix A, we describe the numerical evaluation of the spring tensor by plane-wave expansion. In Appendix B, we outline an alterna-

tive calculation of the spring tensor by partial-wave analysis and multiple scattering. In Appendix C, we delineate and plot the dependence of the spring tensor on the magnitude and the direction of the Bloch wave vector.

II. RIGID CORE-SHELL RESONATORS IN A SOFT ELASTIC MEDIUM

We begin with a brief review of the relevant linear elasticity and elastodynamic equations. We introduce the effective inertia spring tensor (EIST) model for analyzing the acoustic modes and band structure of an array of stiff acoustic resonators in an elastic background.

A. Linear elasticity

In an elastic material at position $\mathbf{x} = (x_1, x_2, x_3)$, the field $\mathbf{u} = (u_1, u_2, u_3)$ describes the displacement of each infinitesimal parcel from the equilibrium. The deformation of the elastic medium is defined locally by the symmetric strain tensor ϵ_{ij} [18]:

$$\epsilon_{ij} = \frac{1}{2} \left(\frac{\partial u_i}{\partial x_j} + \frac{\partial u_j}{\partial x_i} \right), \quad (1)$$

where we neglect the nonlinear correction $(\frac{1}{2}) \sum_k (\partial u_k / \partial x_i) (\partial u_k / \partial x_j)$.

The elastic properties of a linear isotropic elastic material are specified by two free material elastic constants, namely, the Lamé coefficient of bulk deformation λ associated with volume change, and the Lamé coefficient of shear deformation μ associated with lateral distortion. The stress tensor σ_{ij} is linearly proportional to the strain tensor ϵ_{ij} [18]:

$$\sigma_{ij} = C_{ijkl} \epsilon_{kl} = \lambda \text{Tr}(\boldsymbol{\epsilon}) \delta_{ij} + 2\mu \epsilon_{ij}, \quad (2)$$

where $C_{ijkl} = \lambda \delta_{ij} \delta_{kl} + 2\mu \delta_{ik} \delta_{jl}$ is the rank-four stiffness tensor, δ_{ij} is the Kronecker delta function, and Tr is the trace operator. Throughout this paper, repeated indices are summed over by Einstein summation convention.

B. Elastic equations of motion

The equation of motion of the elastic material of density ρ is given by Newton's second law:

$$\rho \frac{\partial^2 u_i}{\partial t^2} = \frac{\partial \sigma_{ij}}{\partial x_j}. \quad (3)$$

For the force per unit volume to be finite everywhere in the material, the stress tensor $\boldsymbol{\sigma}$ must be continuous everywhere. For an isotropic linear elastic solid, Eqs. (2) and (3) yield the dynamical equation

$$\rho \frac{\partial^2 \mathbf{u}_i}{\partial t^2} = \nabla \cdot (\mu \nabla u_i) + \nabla \cdot \left(\mu \frac{\partial \mathbf{u}}{\partial x_i} \right) + \frac{\partial}{\partial x_i} (\lambda \nabla \cdot \mathbf{u}). \quad (4)$$

Here, the elastic Lamé coefficients are locally defined parameters that can vary with position. Despite the material discontinuities of the elastic parameters and the strain tensor, the stress tensor is continuous and differentiable everywhere, corresponding to a finite force on each infinitesimal parcel. This observation is crucial to a convergent plane-wave expansion scheme (see Appendix A). In a homogeneous, isotropic,

linear elastic solid, with material parameters independent of position, the Lamé coefficients can be factored out of the spatial derivatives to yield the conventional elastic wave equation [19].

We express the displacement field in Cartesian coordinates: $\mathbf{u} = u_x \hat{\mathbf{x}} + u_y \hat{\mathbf{y}} + u_z \hat{\mathbf{z}}$. All the specific examples we study in this paper are two dimensional. Monochromatic oscillation at angular frequency ω with temporal dependence $e^{-i\omega t}$ is assumed. The z axis is aligned with direction of translational invariance, and the spatial derivatives with respect to z are null ($\partial/\partial z = 0$). The z component of the displacement field describes transverse out-of-plane oscillation, while the x and y components describe in-plane motion. From Eq. (4), the dynamical equation for out-of-plane displacement simplifies to

$$\frac{\partial}{\partial x} \left(\mu \frac{\partial u_z}{\partial x} \right) + \frac{\partial}{\partial y} \left(\mu \frac{\partial u_z}{\partial y} \right) + \rho \omega^2 u_z = 0. \quad (5)$$

While the in-plane displacement is decoupled from the out-of-plane displacement in Eq. (4), the x component u_x and the y component u_y are intricately coupled:

$$\frac{\partial}{\partial x} \left[(\lambda + 2\mu) \frac{\partial u_x}{\partial x} + \lambda \frac{\partial u_y}{\partial y} \right] + \frac{\partial}{\partial y} \left[\mu \frac{\partial u_x}{\partial y} + \mu \frac{\partial u_y}{\partial x} \right] + \rho \omega^2 u_x = 0, \quad (6a)$$

$$\frac{\partial}{\partial x} \left[\mu \frac{\partial u_x}{\partial y} + \mu \frac{\partial u_y}{\partial x} \right] + \frac{\partial}{\partial y} \left[\lambda \frac{\partial u_x}{\partial x} + (\lambda + 2\mu) \frac{\partial u_y}{\partial y} \right] + \rho \omega^2 u_y = 0. \quad (6b)$$

Consider a resonator contained within a rigid shell of radius R , embedded in a soft elastic background. The strain of the rigid shell is negligible compared to the elastic background. It could be seen from the out-of-plane dynamical equation (5) that the strain inside the rigid medium is inversely proportional to the Lamé parameter $\epsilon_{zx} = (\frac{1}{2}) \partial u_z / \partial x \sim R \rho \omega^2 u_z / \mu$. For example, for a steel cylinder of size $R \approx 1$ cm at A440 tuning pitch, the fractional variation of the out-of-plane displacement is negligible throughout the steel medium: $\Delta u_z / u_z \sim \rho R^2 \omega^2 / \mu \approx 8 \times 10^{-5} \ll 1$. Similarly, from Eqs. (6a) and (6b), the in-plane strain is inversely proportional to the Lamé parameters of the rigid medium. Consequently, in-plane displacements in two orthogonal directions and in-plane rotation are the predominant, low-frequency, macroscopic degrees of freedom of the rigid shell.

The dynamical equations (5), (6a), and (6b) contain second-order spatial and time derivatives. Evaluated on the boundary of the resonator, the spatial derivative terms represent the elastic stress, which when integrated along the boundary yields the total elastic force acting on the resonator shell by the elastic background. On the other hand, the time derivative terms describe the inertial responses of the resonator, including the products of mass density and acceleration. Equations (6a) and (6b) reveal that the in-plane translations in the x and y directions and in-plane rotation of the resonator shell are intricately coupled. In a lattice of rigid shells embedded in soft elastic background, the in-plane translation and rotation of a rigid shell stretches the background to yield a nontrivial in-plane background displacement field $u_x(x, y) \hat{\mathbf{x}} + u_y(x, y) \hat{\mathbf{y}}$. The background simultaneously

exerts nonlocal forces and axial torques on neighboring and distant rigid shells. The spatial dependence of these nonlocal forces and torques is expressed in the form of a wave-vector-dependent “spring tensor.”

C. Effective inertia spring tensor model: Physical picture

The acoustic response of a periodic array of stiff resonators embedded in a soft elastic background is separated into two parts. We first determine the effective, frequency-dependent inertia of the resonator corresponding to each degree of freedom that couples to the background medium. In the cases we study, the resonator has a rigid shell, and the externally coupled degrees of freedom are the translational and angular displacements of the rigid resonator shell. Under a monochromatic disturbance, all internal and external degrees of freedom of the resonator oscillate at the same frequency. The translational and rotational responses of the rigid oscillator shell to forces and torques from the background elastic medium depend on all of the frequency-dependent inertia parameters arising from internal resonances.

Second, we calculate the elastic restoring force acting on the resonator by the background. In a periodic array of resonators with stiff shells embedded in a linear elastic background, the background is governed by an elastodynamic boundary value problem. The elastic restoring force per unit displacement and rotation of the shell is referred to as the spring tensor. It depends on the geometry and the elastic parameters of the background, and is insensitive to the internal degrees of freedom of the resonator. In the three examples we study below, the resonator in each case occupies the same regions of space. Accordingly, the same spring tensor applies in each example. In a periodic system of resonators, it is convenient to express the response in terms of Fourier components at each possible wave vector \mathbf{K} rather than at the location of a single oscillator.

The resulting EIST model provides a powerful and precise physical representation of the low-frequency behavior of a complex acoustic metamaterial. This is an important generalization of the simple mass-in-a-box picture that accurately recaptures the effect of coupling between multiple resonances at one location with those at other locations.

We calculate the acoustic band structure by relating the effective inertia of the resonator and the elastic restoration due to the background, in a generic form of Newton’s second law:

$$M_{e,i}(f) \ddot{X}_i = -k_{b,ij}(\mathbf{K}) X_j. \quad (7)$$

Here, X_i denotes the set of deviations from equilibrium of the i th degree of freedom (translational or rotational) at a particular wave vector \mathbf{K} , $f \equiv \omega/(2\pi)$ is the frequency measured in hertz, $M_{e,i}(f)$ denotes the effective, frequency-dependent inertia of the resonator associated with the generalized displacement X_i , and $k_{b,ij}$ is the generalized force acting on the resonator by the background in the i th variable, per unit displacement of the j th variable. The force on a given resonator depends on the displacements of all other resonators in the lattice, and the Bloch wave vector \mathbf{K} defines their relative displacements. In two-dimensional structures, the out-of-plane motion is decoupled from the in-plane motion. The out-of-plane response of the resonator is described by an effective

mass $M_{e,z}(f)$, corresponding to out-of-plane translational oscillation at frequency f and amplitude Z . The out-of-plane oscillations of the resonators couple with the out-of-plane oscillations of the neighboring resonators through the elastic background, giving rise to the background spring tensor component $k_{b,zz}(\mathbf{K})$. The out-of-plane mode spectrum $f(\mathbf{K})$ is obtained from the simple harmonic oscillator equation for oscillation at the particular frequency f :

$$-4\pi^2 f^2 M_{e,z}(f)Z = -k_{b,zz}(\mathbf{K})Z. \quad (8)$$

The in-plane response of the resonator is described by a set of three inertial quantities, effective masses $M_{e,x/y}(f)$ for in-plane translational oscillation at frequency f and amplitude X/Y , and effective moment of inertia $I_e(f)$ for in-plane rotational oscillation at frequency f and amplitude Ψ . The in-plane translations and rotation are intricately coupled, in a way that the in-plane translation or rotation of a resonator generally excites simultaneously the translations in two orthogonal directions and the rotation of the neighboring units. The background spring constants $k_{b,ij}(\mathbf{K})$ constitute a 3×3 matrix. The in-plane mode spectrum $f(\mathbf{K})$ is obtained from a set of coupled simple harmonic oscillator equations for oscillation at the particular frequency f :

$$\begin{aligned} & -4\pi^2 f^2 \begin{pmatrix} M_{e,x}(f)X \\ M_{e,y}(f)Y \\ I_e(f)\Psi \end{pmatrix} \\ & = - \begin{pmatrix} k_{b,xx}(\mathbf{K}) & k_{b,xy}(\mathbf{K}) & k_{b,x\psi}(\mathbf{K}) \\ k_{b,yx}(\mathbf{K}) & k_{b,yy}(\mathbf{K}) & k_{b,y\psi}(\mathbf{K}) \\ k_{b,\psi x}(\mathbf{K}) & k_{b,\psi y}(\mathbf{K}) & k_{b,\psi\psi}(\mathbf{K}) \end{pmatrix} \begin{pmatrix} X \\ Y \\ \Psi \end{pmatrix}. \end{aligned} \quad (9)$$

The low-frequency band structure calculation is reduced from a theoretically infinite-dimensional eigenvalue problem to solving a finite-dimensional matrix equation. The condition for a nontrivial solution leads to a polynomial equation for f at each value of \mathbf{K} . Band gaps correspond to frequency ranges where the effective inertia is negative, when Newton's second law admits no real solution in frequency. Not only is this approach computationally efficient, but it also provides a clear physical picture of the acoustic modes and band gaps.

III. EXAMPLE A: NONRESONANT UNIFORM CYLINDERS

We first consider the acoustic band structure of a square lattice of uniform right, circular, cellulose cylinders in open-cell foam. This leads to an evaluation of the background spring tensor that is used also in examples B and C involving nonuniform resonant cylinders. The cellulose cylinders are orders of magnitude stiffer than the background foam, and effectively act as rigid bodies. The out-of-plane bands arise from the interaction between the out-of-plane translational oscillations of the cylinders. The in-plane bands are the coupled in-plane translation and rotation of the solid cylinders. The inertial response of the cellulose cylinders are fully described by their masses and moments of inertia. The band structures recaptured by simple algebraic equations for the frequency $f(\mathbf{K})$ in our EIST model agree, within 1.8% accuracy, with finite-element method calculations. The background spring tensor derived in model A is applied to models B and C in subsequent sections.

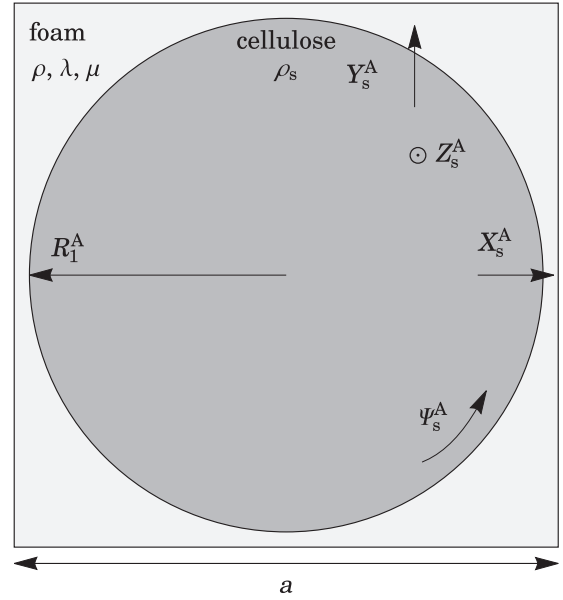


FIG. 1. In model A, the nonresonant unit cell consists of circular cellulose cylinder of radius $R_1^A \approx 0.4720$ cm embedded in open cell foam. The rigid cellulose cylinder has four mechanical degrees of freedom, namely, translation in the $x/y/z$ direction $X_s^A/Y_s^A/Z_s^A$ and axial rotation Ψ_s^A .

A. Model A

We consider a square-lattice phononic crystal consisting of right, circular, cellulose, cylinders with lattice constant $a = 1$ cm. The background is filled with open-cell foam. The cellulose cylinders fill $\phi_c^A = 70\%$ by volume, so that the radius of each cylinder is $R_1^A = \sqrt{\phi_c^A/\pi} = 0.4720$ cm. The unit cell is depicted in Fig. 1. The relevant material parameters are listed in Table I.

The cellulose cylinder acts as a rigid body, and has four mechanical degrees of freedom in two dimensions. The cellulose cylinder displaces in-plane in the x/y direction by X_s^A/Y_s^A , displaces out-of-plane in the z direction by Z_s^A , and rotates counterclockwise by Ψ_s^A , from the equilibrium position. The

TABLE I. Tabulated are the density ρ and Lamé parameters (λ, μ) of the pertinent elastic medium. The mechanical data of steel are adopted from sample number 11 of the experimental collection of 20 samples of steel which show small variations of 0.5%, 1.8%, and 0.9% in ρ, λ , and μ , respectively [20]. Cellulose represents cellulose nitrate thermoplastics that is a common material for ping-pong balls [21]. Its excellent machinability facilitates molding into stiff resonator shell. Open-cell foam corresponds to type A foam manufactured by Foamex International Inc. [22] It contains 0.4-mm pores with 60 pores per inch. The foam is approximated as an isotropic solid by ignoring the modest anisotropy ratio of 1.0 : 1.1 : 1.4 in the mechanical moduli.

Material	ρ (kg m ⁻³)	λ (Pa)	μ (Pa)
Steel [20]	7940	1.075×10^{11}	7.815×10^{10}
Cellulose [21]	1350	1.21×10^9	5.19×10^8
Open-cell foam [22]	30	2.31×10^4	1.538×10^4

mass M_s^A and the moment of inertia I_s^A per unit length in the transverse direction are given by

$$M_s^A = \rho_s \pi (R_1^A)^2 \approx 0.09450 \text{ kg m}^{-1}, \quad (10a)$$

$$I_s^A = \frac{1}{2} \rho_s \pi (R_1^A)^4 \approx 1.053 \times 10^{-6} \text{ kg m}. \quad (10b)$$

The equations of motion of the rigid cylinder are given by

$$M_s^A \ddot{X}_s^A = F_{b,x}(\mathbf{K}), \quad (11a)$$

$$M_s^A \ddot{Y}_s^A = F_{b,y}(\mathbf{K}), \quad (11b)$$

$$M_s^A \ddot{Z}_s^A = F_{b,z}(\mathbf{K}), \quad (11c)$$

$$I_s^A \ddot{\Psi}_s^A = \tau_b(\mathbf{K}), \quad (11d)$$

where $F_{b,x/y/z}(\mathbf{K})$ [$\tau_b(\mathbf{K})$] denotes the force in the $x/y/z$ direction (axial torque) acting on the rigid cellulose cylinder by the background foam. In this nonresonant model, the effective mass is identical in three orthogonal directions, and all inertial parameters are independent of frequency.

B. Background spring tensor

The elastic restoration force due to the background foam depends on the deformation caused by the (angular) displacement of the cylinder. In linear elasticity, the restoring force and torque are directly proportional to the displacement of the cylinder. In two dimensions, the out-of-plane oscillation is decoupled from the in-plane motion, so that the force $F_{b,z}(\mathbf{K})$ acting on the cylinder by the background in the z direction depends only on the out-of-plane displacement Z_s^A . We define the associated spring constants $k_{b,zz}$:

$$k_{b,zz}(\mathbf{K}) = -\frac{F_{b,z}(\mathbf{K})}{Z_s^A}. \quad (12)$$

On the other hand, the in-plane translation and rotation are intricately coupled. The in-plane forces $F_{b,x/y}(\mathbf{K})$ and the axial torque $\tau_{b,z}(\mathbf{K})$ acting on the rigid cylinder by the background foam depend jointly on the in-plane translation X_s^A and Y_s^A and rotation Ψ_s^A :

$$\begin{pmatrix} F_{b,x}(\mathbf{K}) \\ F_{b,y}(\mathbf{K}) \\ \tau_{b,\psi}(\mathbf{K}) \end{pmatrix} = - \begin{pmatrix} k_{b,xx}(\mathbf{K}) & k_{b,xy}(\mathbf{K}) & k_{b,x\psi}(\mathbf{K}) \\ k_{b,yx}(\mathbf{K}) & k_{b,yy}(\mathbf{K}) & k_{b,y\psi}(\mathbf{K}) \\ k_{b,\psi x}(\mathbf{K}) & k_{b,\psi y}(\mathbf{K}) & k_{b,\psi\psi}(\mathbf{K}) \end{pmatrix} \begin{pmatrix} X_s^A \\ Y_s^A \\ \Psi_s^A \end{pmatrix}. \quad (13)$$

Here, $k_{b,ij}(\mathbf{K})$ is the spring tensor at wave vector \mathbf{K} , denoting the force and torque acting on the cylinder in the direction of the i variable, per unit displacement of the j variable. The calculations of the spring tensor by plane-wave expansion and multiple scattering of partial waves are described in Appendices A and B, respectively.

The out-of-plane spring constant $k_{b,zz}$ is plotted along a triangular path $M \rightarrow \Gamma \rightarrow X \rightarrow M$ in the first Brillouin zone in Fig. 2. The behavior of the spring tensor as a function of the magnitude K and orientation ϕ of the wave vector $\mathbf{K} = K(\cos\phi\hat{x} + \sin\phi\hat{y})$ is depicted Figs. 3(a) and 3(b). At a fixed magnitude of the wave vector, the spring tensor is a periodic function in ϕ with period 2π . We introduce the Fourier

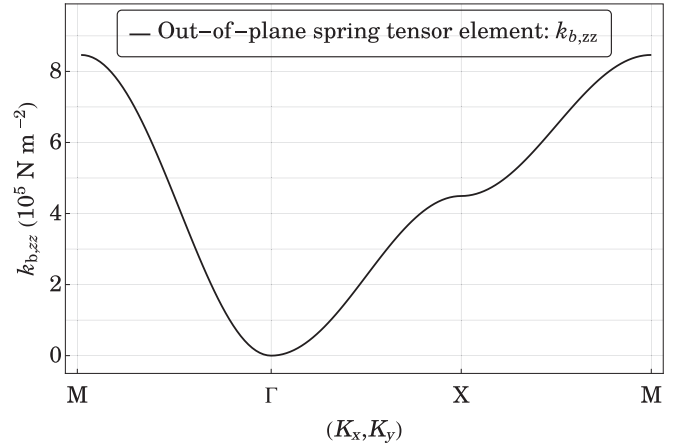


FIG. 2. The spring tensor component for out-of-plane translation is plotted in the first Brillouin zone along the path $M \rightarrow \Gamma \rightarrow X \rightarrow M$.

coefficients c_n^{ij} and s_n^{ij} to describe the angular dependence of a spring tensor component $k_{b,ij}$:

$$c_0^{ij}(K) = \frac{1}{2\pi} \int_0^{2\pi} k_{b,ij}(K, \phi) d\phi, \quad (14a)$$

$$c_n^{ij}(K) = \frac{1}{\pi} \int_0^{2\pi} k_{b,ij}(K, \phi) \cos(n\phi) d\phi, \quad (14b)$$

$$s_n^{ij}(K) = \frac{1}{\pi} \int_0^{2\pi} k_{b,ij}(K, \phi) \sin(n\phi) d\phi, \quad (14c)$$

where n is an arbitrary positive integer. As such, the spring tensor can be expressed in a Fourier series in the wave-vector angle ϕ :

$$k_{b,ij}(K, \phi) = c_0^{ij}(K) + \sum_{n=1}^{\infty} c_n^{ij}(K) \cos(n\phi) + s_n^{ij}(K) \sin(n\phi). \quad (14d)$$

Near the center of the Brillouin zone, $k_{b,zz}$ is insensitive to the orientation of the wave vector. The fourth harmonic associated with $\cos(4\phi)$ emerges near the edge of the Brillouin zone. Other harmonics vanish by fourfold rotational symmetry of the lattice. Graphs illustrating the dependence of other components of the spring tensor on the magnitude and the direction of the wave vector \mathbf{K} are provided in Appendix C. From here on, the subscript b , denoting the background, is dropped for the rank-two spring tensor, when no ambiguity arises.

C. Acoustic band structure in the EIST model

Given the background spring tensor, the acoustic dispersion relations $f(\mathbf{K})$ are determined by the roots of a polynomial equation in f^2 . By Eqs. (11c) and (12), the first out-of-plane band arises from the coupling of the out-of-plane translational oscillation of the cellulose cylinders:

$$-4\pi^2 M_s^A f^2(\mathbf{K}) = -k_{zz}(\mathbf{K}). \quad (15)$$

Similarly, by Eqs. (11a), (11b), (11d), and (13), the first three in-plane bands are associated with the cou-

under plane translation and rotation between the cellulose

$$\det \begin{pmatrix} k_{xx}(\mathbf{K}) - 4\pi^2 M_s^A f^2(\mathbf{K}) & k_{xy}(\mathbf{K}) & k_{x\psi}(\mathbf{K}) \\ k_{yx}(\mathbf{K}) & k_{yy}(\mathbf{K}) - 4\pi^2 M_s^A f^2(\mathbf{K}) & k_{y\psi}(\mathbf{K}) \\ k_{\psi x}(\mathbf{K}) & k_{\psi y}(\mathbf{K}) & k_{\psi\psi}(\mathbf{K}) - 4\pi^2 I_s^A f^2(\mathbf{K}) \end{pmatrix} = 0. \quad (16)$$

Here, \det denotes the determinant of a matrix. The out-of-plane and in-plane band structures are plotted in Figs. 4 and 5, respectively. The maximum percentage deviation from the exact finite-element method benchmark is 0.69% for the first out-of-plane band, and 1.8% for the first three in-plane bands. The next acoustic band occurs at frequency beyond 3000 Hz.

The close numerical agreement reveals that the rigid shell approximation applies. The eigenfrequencies are accurately

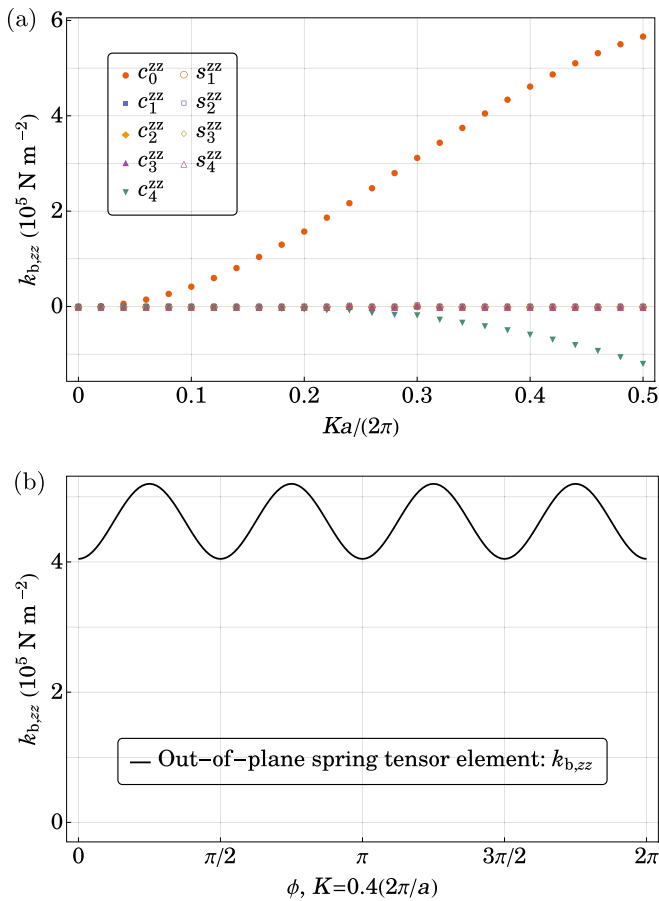


FIG. 3. Dependence of the spring tensor component $k_{b,zz}$ for out-of-plane translational oscillation on the magnitude and orientation of the Bloch wave vector \mathbf{K} . (a) The Fourier coefficients (up to the fourth harmonics) of the spring tensor component for out-of-plane translation is plotted from the center of the first Brillouin zone to the radius of the largest inscribed circle at $K = 0.5(2\pi/a)$. Here, c_n^{zz} and s_n^{zz} denote the Fourier coefficients of $k_{b,zz}$ associated with $\cos(n\phi)$ and $\sin(n\phi)$, respectively. (b) The spring tensor component $k_{b,zz}$ for out-of-plane translational oscillation is plotted as a function of the orientation ϕ of the wave vector at a fixed magnitude $K = 0.4(2\pi/a)$. $k_{b,zz}$ is predominated by the zeroth and the fourth harmonics.

recaptured by simple polynomial equations in f^2 for the out-of-plane and in-plane bands. The nontrivial coupling between the in-plane translational and rotational modes is apparent by tracing the third band continuously from the nondegenerate rotational mode at Γ to the degenerate translational modes at M . Both the mass and the moment of inertia are essential effective inertial parameters of the rigid cellulose cylinder. In this nonresonant model, all inertial parameters are frequency independent. The dimensionless moment of inertia factor assumes the value of a uniform solid cylinder $I^A/[M^A(R^A)^2] = 1/2$. In subsequent locally resonant models, the inertial parameters are frequency dependent. As discussed in Secs. IV and V, this leads to higher-order polynomial equations for the dispersion relations $f(\mathbf{K})$.

IV. EXAMPLE B: LOCALLY RESONANT CORE-SHELL UNIT

We now consider the acoustic band structure of a square lattice of right, circular steel cylinders, encapsulated by coaxial cellulose shell, surrounded by open-cell foam. Local resonance occurs within the resonators because of the relative motion between the steel core and the cellulose shell. The inertial response of each resonator is described by its effective, frequency-dependent out-of-plane mass, in-plane mass, and moment of inertia, derived by expressing the internal degrees of freedom as frequency-dependent inertia, as discussed below. The band structures are calculated by solving polynomial equations in the square of frequency f^2 , using the effective masses, moment of inertia, and the wave-vector-dependent

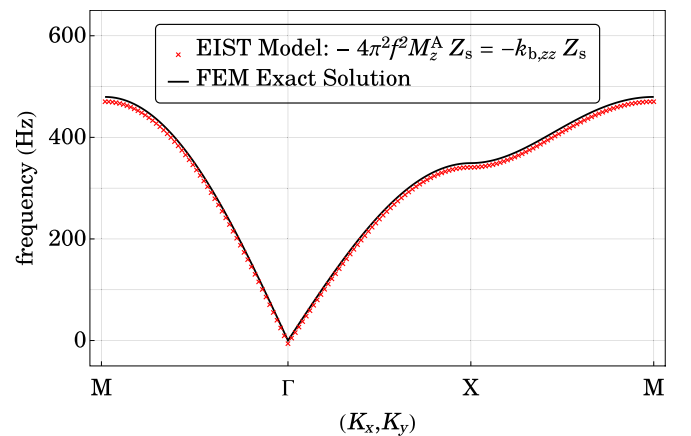


FIG. 4. The lowest-frequency out-of-plane acoustic band of the periodic cellulose-foam composite (model A) is plotted in the first Brillouin zone along the path $M \rightarrow \Gamma \rightarrow X \rightarrow M$, for the algebraic method (red crosses) in Eq. (15). The finite-element method (solid black line) is used to calculate the out-of-plane bands of the actual phononic crystal. The maximum percentage error is 0.69%.

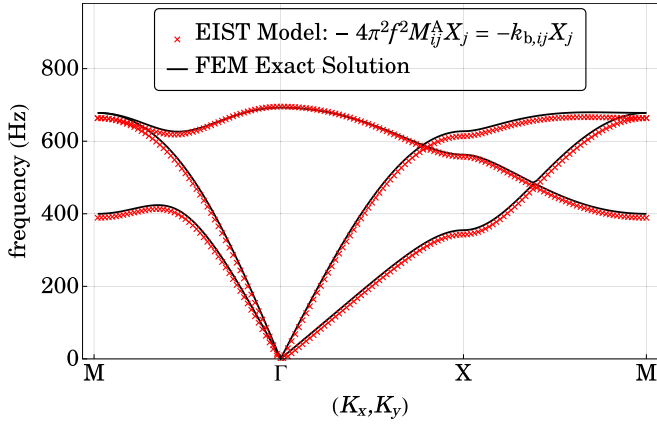


FIG. 5. The first three in-plane acoustic bands of the periodic cellulose-foam composite (model A) is plotted in the first Brillouin zone along the path $M \rightarrow \Gamma \rightarrow X \rightarrow M$ for the algebraic method (red crosses) in Eq. (16). The finite-element method (solid black line) is used to calculate the in-plane bands of the actual phononic crystal. The maximum relative error is 1.8%.

spring tensor from Sec. III. The results agree, within 4.0%, with finite-element method calculations. Previously [9], the same resonant structure was studied using cutting surface method (CSM), which failed to recapture the in-plane bands, involving intricate coupling between translational and rotational resonances at different locations. The incorporation of the wave-vector-dependent spring tensor enables a proper treatment of these couplings and leads to a nearly exact band structure.

A. Model B

A square-lattice phononic crystal consisting of circular steel rods, with lattice constant $a = 1$ cm, is considered. Each circular steel rod is coupled to a stiff circular cellulose shell via open-cell foam. The background, exterior to the cellulose shell, is the same type of open-cell foam. The steel core, cellulose shell, and the interstitial foam between the core and the shell fill $\phi_c^B = 20\%$, $\phi_s^B = 20\%$, and $\phi_f^B = 30\%$ by volume, respectively, so that the radius of the circular steel rod $R_1^B = a\sqrt{\phi_c^B/\pi} \approx 0.2523$ cm, the inner radius of the circular cellulose shell $R_2^B = a\sqrt{(\phi_c^B + \phi_f^B)/\pi} \approx 0.3989$ cm, and the outer radius $R_3^B = a\sqrt{(\phi_c^B + \phi_f^B + \phi_s^B)/\pi} \approx 0.4720$ cm. The unit cell is depicted in Fig. 6. The density of the steel core ρ_c and that of the cellulose shell ρ_s are provided in Table I.

The steel core and the cellulose shell are elastically much stiffer than the interstitial open-cell foam. The stiff core and shell are approximated as rigid bodies with four mechanical degrees of freedom each. The steel core (cellulose shell) displaces in plane in the x/y direction by X_c^B/Y_c^B (X_s^B/Y_s^B), displaces out-of-plane in the z direction by Z_c^B (Z_s^B), and rotates counterclockwise by Ψ_c^B (Ψ_s^B) from the equilibrium position. The mass per unit length of the steel core M_c^B and that of the cellulose shell M_s^B are given by

$$M_c^B = \rho_c \pi (R_1^B)^2 \approx 0.1588 \text{ kg m}^{-1}, \quad (17a)$$

$$M_s^B = \rho_s \pi [(R_3^B)^2 - (R_2^B)^2] \approx 0.02700 \text{ kg m}^{-1}. \quad (17b)$$

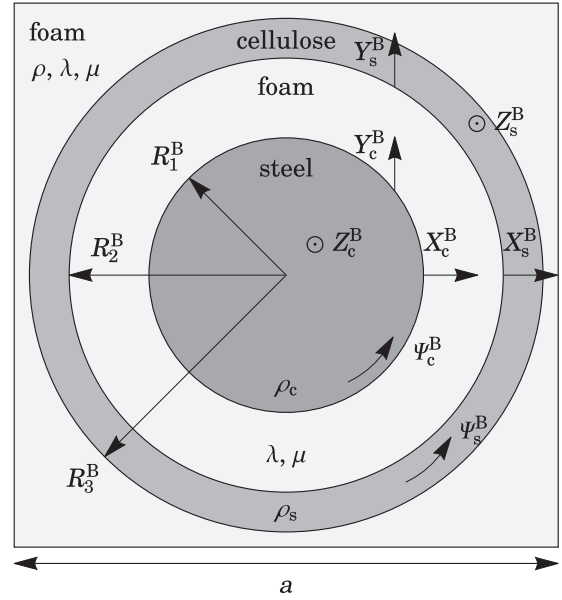


FIG. 6. A unit cell in model B consists of a dense steel rod of radius $R_1^B \approx 0.2523$ cm surrounded by a concentric, circular cellulose shell of inner radius $R_2^B \approx 0.3989$ cm and outer radius $R_3^B \approx 0.4720$ cm with the interstitial spaces filled with open-cell foam. The unit cells are arranged in a square lattice of lattice constant $a = 1$ cm. The unit cell is described by eight mechanical degrees of freedom, including the translation in the $x/y/z$ direction $X_c^B/Y_c^B/Z_c^B$ and axial rotation Ψ_c^B of the interior steel core, as well as the corresponding variables X_s^B, Y_s^B, Z_s^B , and Ψ_s^B of the exterior cellulose shell.

Similarly, the moment of inertia per unit length of the steel core I_c^B and that of the cellulose shell I_s^B are given by

$$I_c^B = \frac{\pi}{2} \rho_c (R_1^B)^4 \approx 0.5055 \times 10^{-6} \text{ kg m}, \quad (18a)$$

$$I_s^B = \frac{\pi}{2} \rho_s [(R_3^B)^4 - (R_2^B)^4] \approx 0.5157 \times 10^{-6} \text{ kg m}. \quad (18b)$$

The equations of motion are given by

$$M_c^B \ddot{X}_c^B = F_{c,x}^B, \quad (19a)$$

$$M_s^B \ddot{X}_s^B = F_{s,x}^B + F_{b,x}, \quad (19b)$$

$$M_c^B \ddot{Y}_c^B = F_{c,y}^B, \quad (19c)$$

$$M_s^B \ddot{Y}_s^B = F_{s,y}^B + F_{b,y}, \quad (19d)$$

$$M_c^B \ddot{Z}_c^B = F_{c,z}^B, \quad (19e)$$

$$M_s^B \ddot{Z}_s^B = F_{s,z}^B + F_{b,z}, \quad (19f)$$

$$I_c^B \ddot{\Psi}_c^B = \tau_c^B, \quad (19g)$$

$$I_s^B \ddot{\Psi}_s^B = \tau_s^B + \tau_b. \quad (19h)$$

Here, $\mathbf{F}_{c/s}^B = F_{c/s,x}^B \hat{\mathbf{x}} + F_{c/s,y}^B \hat{\mathbf{y}} + F_{c/s,z}^B \hat{\mathbf{z}}$ and $\boldsymbol{\tau}_{c/s}^B = \tau_{c/s}^B \hat{\mathbf{z}}$ denote the force and the torque per unit length acting on the steel core and cellulose shell by the interstitial foam, respectively.

The interstitial foam essentially acts like an elastic spring, harmonically coupling the steel core and the cellulose shell. When the elastic wavelength is much longer than the size of the resonant units, wave phenomena within each resonant unit

can be neglected using an elastostatic approximation. Under the rigid core-shell approximations (RCSA), the region of the interstitial foam satisfies elastostatic equilibrium under appropriate boundary conditions specified by the relative displacements of the rigid bodies [9,23]. The elastic restoring forces due to the foam satisfy Hooke's law:

$$F_{c,x}^B = -F_{s,x}^B = k_x^B (X_s^B - X_c^B), \quad (20a)$$

$$F_{c,y}^B = -F_{s,y}^B = k_y^B (Y_s^B - Y_c^B), \quad (20b)$$

$$F_{c,z}^B = -F_{s,z}^B = k_z^B (Z_s^B - Z_c^B), \quad (20c)$$

$$\tau_c^B = -\tau_s^B = k_\psi^B (\Psi_s^B - \Psi_c^B), \quad (20d)$$

where the spring constants depend on the geometry and the Lamé parameters (λ , μ) of the foam [9]:

$$k_x^B = k_y^B = 4\pi\mu(\lambda + 2\mu)(\lambda + 3\mu)[(R_1^B)^2 + (R_2^B)^2] / \{(\lambda + 3\mu)^2[(R_1^B)^2 + (R_2^B)^2] \ln R_2^B/R_1^B - (\lambda + \mu)^2[(R_2^B)^2 - (R_1^B)^2]\} \approx 4.615 \times 10^5 \text{ N m}^{-2}, \quad (21a)$$

$$k_z^B = \frac{2\pi\mu}{\ln R_2^B/R_1^B} \approx 2.109 \times 10^5 \text{ N m}^{-2}, \quad (21b)$$

$$k_\psi^B = \frac{4\pi\mu(R_1^B)^2(R_2^B)^2}{(R_2^B)^2 - (R_1^B)^2} \approx 2.051 \text{ N}. \quad (21c)$$

B. Single-resonance effective mass

The equations of motion of the in-plane rotation and translation in three orthogonal directions could be mapped to individual one-dimensional spring-mass models introduced previously [11,24]. A rigid box of mass m_1 with displacement x_1 contains a point mass m_2 with displacement x_2 held by a spring with stiffness constant k , and responds to an external harmonic force $F(f)$. This response is governed by the equations of motion

$$m_1 \ddot{x}_1 = F(f) + k(x_2 - x_1), \quad (22a)$$

$$m_2 \ddot{x}_2 = k(x_1 - x_2). \quad (22b)$$

We introduce the natural frequency $f_0 = (1/2\pi)\sqrt{k/m_2}$. Under the external harmonic force, both masses oscillate at the same frequency f . By rearranging Eq. (22b), we find that the motion of the interior mass is proportional to that of the box:

$$x_2 = \left(\frac{f_0^2}{f_0^2 - f^2} \right) x_1. \quad (23)$$

Equation (23) is substituted into Eq. (22a) to reduce the system of coupled differential equations into a single-variable equation for oscillation at frequency f :

$$\left(m_1 + \frac{m_2 f_0^2}{f_0^2 - f^2} \right) \ddot{x}_1 = F(f). \quad (24)$$

The coefficient of the second time derivative of the displacement of the shell is interpreted as an *effective, frequency-*

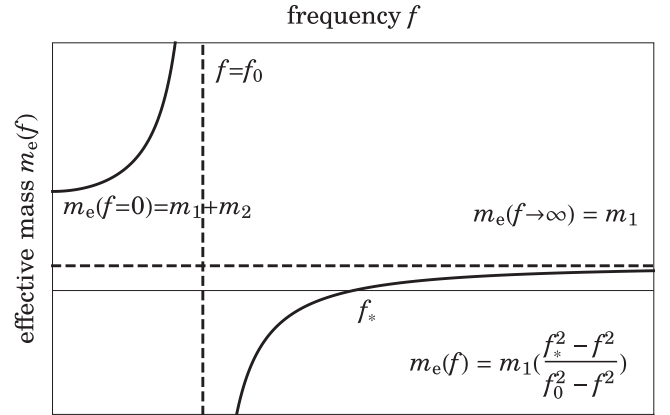


FIG. 7. Nondissipative, frequency-dependent effective mass in Eq. (25) is schematically plotted. Note that the effective mass diverges at $f = f_0$, and is negative over the range $f_0 < f < f_*$.

dependent mass $m_e(f)$ of the locally resonant unit [11]:

$$m_e(f) = m_1 + \frac{m_2 f_0^2}{f_0^2 - f^2} = m_1 \left(\frac{f_*^2 - f^2}{f_0^2 - f^2} \right), \quad (25)$$

where f_* is the frequency at which the effective mass vanishes:

$$f_* = f_0 \left(1 + \frac{m_2}{m_1} \right)^{1/2} = \frac{1}{2\pi} \left(\frac{k}{m_1} + \frac{k}{m_2} \right)^{1/2}. \quad (26)$$

This is plotted as a function of frequency in Fig. 7. The effective mass increases from the total mass of the system at zero frequency to infinity at the resonant frequency f_0 . Over the frequency range $f_0 < f < f_*$, the effective mass is negative, and wave propagation is inhibited over such frequency range. Beyond that, the effective mass increases from zero at f_* to the mass of the box in the high-frequency limit.

Under the RCSA, the interstitial foam acts as a Hookean spring (20a)–(20d), and the coupled equations of motion for each pair of degrees of freedom in (19a)–(19h) are mapped to one-dimensional mass-in-a-box models in (22a) and (22b). Readers can refer to Tables II, III, and IV in [9] for the correspondence of each physical variable of the resonator and the spring-mass model. Hence, the resonant unit is described by the frequency-dependent, effective masses $M_{x,e}^B(f)$ and $M_{y,e}^B(f)$ for in-plane translations, effective mass $M_{z,e}^B(f)$ for out-of-plane translation, and the effective moment of inertia $I_e^B(f)$ for in-plane rotation:

$$M_{x,e}^B(f) = M_{y,e}^B(f) = M_s^B \left(\frac{f_{*,t}^B - f^2}{f_{0,t}^B - f^2} \right), \quad (27a)$$

$$M_{z,e}^B(f) = M_s^B \left(\frac{f_{*,z}^B - f^2}{f_{0,z}^B - f^2} \right), \quad (27b)$$

$$I_e^B(f) = I_s^B \left(\frac{f_{*,r}^B - f^2}{f_{0,r}^B - f^2} \right). \quad (27c)$$

Here, the resonant frequencies of in-plane translation $f_{0,t}^B$, out-of-plane translation $f_{0,z}^B$, and in-plane rotation

$f_{0,r}^B$ are

$$f_{0,t}^B = (1/2\pi)(k_x^B/M_c^B)^{1/2} \approx 271.3 \text{ Hz}, \quad (28a)$$

$$f_{0,z}^B = (1/2\pi)(k_z^B/M_c^B)^{1/2} \approx 183.4 \text{ Hz}, \quad (28b)$$

$$f_{0,r}^B = (1/2\pi)(k_\psi^B/I_c^B)^{1/2} \approx 320.6 \text{ Hz}. \quad (28c)$$

The zero-effective density frequencies for in-plane translation $f_{*,t}^B$, out-of-plane translation $f_{*,z}^B$, and in-plane rotation $f_{*,r}^B$ are

$$f_{*,t}^B = (1/2\pi)(k_x^B/M_c^B + k_x^B/M_s^B)^{1/2} \approx 711.7 \text{ Hz}, \quad (29a)$$

$$f_{*,z}^B = (1/2\pi)(k_z^B/M_c^B + k_z^B/M_s^B)^{1/2} \approx 481.2 \text{ Hz}, \quad (29b)$$

$$f_{*,r}^B = (1/2\pi)(k_\psi^B/I_c^B + k_\psi^B/I_s^B)^{1/2} \approx 451.1 \text{ Hz}. \quad (29c)$$

C. Acoustic band structure in the EIST model

In linear elasticity, the elastic restoration forces are uniquely determined by the boundary conditions. If the shell of a resonator is orders of magnitude stiffer than the open-cell foam background, the boundary conditions of the elastic foam medium are predominated by the translation and the rotation of the rigid cellulose shell. As the steel-core resonators in model B occupy the same volume as the cellulose cylinders in model A, embedded in the same background foam, the same background spring tensor applies.

By Eqs. (19e), (19f), and (27b), the out-of-plane eigenfrequency $f(\mathbf{K})$ in the EIST model is governed by

$$4\pi^2 M_{z,e}^B(f) f^2 = k_{zz}(\mathbf{K}). \quad (30)$$

This quadratic equation in f^2 yields a pair of non-negative solutions:

$$f_{\pm}(\mathbf{K}) = \left\{ \frac{f_{*,z}^2}{2} + \frac{k_{zz}(\mathbf{K})}{8\pi^2 M_s^B} \pm \left[\left(\frac{f_{*,z}^2}{2} + \frac{k_{zz}(\mathbf{K})}{8\pi^2 M_s^B} \right)^2 - \frac{f_{0,z}^2 k_{zz}(\mathbf{K})}{4\pi^2 M_s^B} \right]^{1/2} \right\}^{1/2}. \quad (31)$$

The first two out-of-plane acoustic bands are plotted in Fig. 8. Graphically, at each wave vector \mathbf{K} , the left-hand side

$$4\pi^2 f^2 \begin{pmatrix} M_{x,e}^B(f) X_s^B \\ M_{y,e}^B(f) Y_s^B \\ I_e^B(f) \Psi_s^B \end{pmatrix} = \begin{pmatrix} k_{xx}(\mathbf{K}) & k_{xy}(\mathbf{K}) & k_{x\psi}(\mathbf{K}) \\ k_{yx}(\mathbf{K}) & k_{yy}(\mathbf{K}) & k_{y\psi}(\mathbf{K}) \\ k_{\psi x}(\mathbf{K}) & k_{\psi y}(\mathbf{K}) & k_{\psi\psi}(\mathbf{K}) \end{pmatrix} \begin{pmatrix} X_s^B \\ Y_s^B \\ \Psi_s^B \end{pmatrix}. \quad (32)$$

Determination of the in-plane eigenfrequencies amounts to solving a degree-six polynomial equation in f^2 :

$$\det \begin{pmatrix} k_{xx}(\mathbf{K}) - 4\pi^2 f^2 M_{x,e}^B(f) & k_{xy}(\mathbf{K}) & k_{x\psi}(\mathbf{K}) \\ k_{yx}(\mathbf{K}) & k_{yy}(\mathbf{K}) - 4\pi^2 f^2 M_{y,e}^B(f) & k_{y\psi}(\mathbf{K}) \\ k_{\psi x}(\mathbf{K}) & k_{\psi y}(\mathbf{K}) & k_{\psi\psi}(\mathbf{K}) - 4\pi^2 f^2 I_e^B(f) \end{pmatrix} = 0. \quad (33)$$

The first six in-plane acoustic bands are plotted in Fig. 9. Qualitatively, the simple pole in the frequency-dependent, effective masses and moment of inertia split the three in-plane bands in the nonresonant case (model A) into six planar bands. In the first two bands, the in-plane translation and rotation of the steel core and the cellulose shell are in phase. The observed band gap from 303.4 to 668.9 Hz includes the fre-

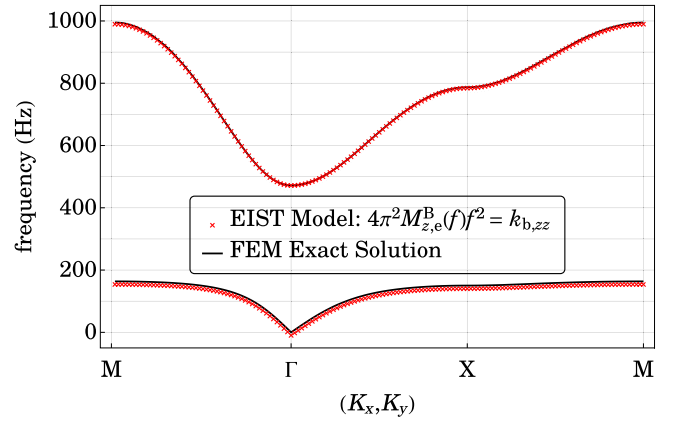


FIG. 8. The first two out-of-plane acoustic bands of the periodic steel-cellulose-foam locally resonant composite (model B) are plotted in the first Brillouin zone along the path $M \rightarrow \Gamma \rightarrow X \rightarrow M$, using the algebraic solution (red crosses) of the EIST model in Eq. (31). The finite-element method (solid black line) is used to calculate the exact out-of-plane bands of the original phononic crystal. The maximum percentage error is 1.9%.

in Eq. (30) increases from zero at $f = 0$ to infinity at the resonant frequency $f = f_{0,z}$. Over this frequency range $0 \leq f < f_{0,z}$, it intersects exactly once with the non-negative out-of-plane background spring tensor component $k_{zz}(\mathbf{K})$. This gives rise to the first out-of-plane acoustic band $f_-(\mathbf{K})$. The steel core and the cellulose shell oscillate in phase in the lower-frequency band. Over the frequency range $f_{0,z} < f < f_{*,z}$, the left-hand side is negative, so that no interaction occurs. This corresponds to an acoustic band gap. Beyond the zero density frequency $f > f_{*,z}$, the left-hand side increases monotonically without bound from 0 at $f = f_{*,z}$, which gives rise to another intersection associated with the second out-of-plane acoustic band $f_+(\mathbf{K})$. The steel core and the cellulose shell oscillate in antiphase in the upper frequency band.

By Eqs. (19a)–(19d), (19g), (19h), (27a), and (27c), the in-plane bands are governed by the nonlinear matrix eigenvalue equation

quency range $f_{0,r}^B < f < f_{*,r}^B$ over which the effective in-plane mass and moment of inertia are simultaneously negative. In the three upper bands, the in-plane translation and rotation of the steel core and the cellulose shell are in antiphase.

Both the effective mass and the moment of inertia are necessary to recapture the in-plane motion. The requirement of a frequency-dependent moment of inertia is often overlooked in

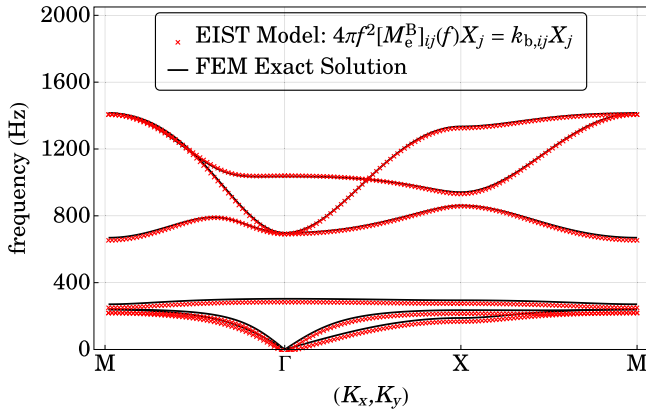


FIG. 9. The first six in-plane acoustic bands of the periodic, locally resonant steel-cellulose-foam composite (model B) are plotted in the first Brillouin zone along the path $M \rightarrow \Gamma \rightarrow X \rightarrow M$, for the algebraic EIST model solution (red crosses) of Eq. (32). The finite-element method (solid black line) is used to calculate the in-plane bands of the actual phononic crystal. The maximum relative error is 4.0%.

the literature. Over the bulk of the third band $270.7 \text{ Hz} < f < 303.4 \text{ Hz}$, the in-plane mass is negative while the in-plane moment of inertia is positive. This suggests that the third band is heavily influenced by the coupled in-phase rotational oscillations of the steel core and the cellulose shell. Wave propagation is still permitted at negative effective mass if the effective moment of inertia is positive.

It is impossible to fully recapture the in-plane bands by the previously used cutting surface method (CSM) [9,10]. In the CSM, the resonant unit with a single frequency-dependent effective mass is replaced by a medium of uniform effective density, and a hypothetical set of acoustic dispersion relations $\tilde{f}(\mathbf{K}, \rho_p)$ is evaluated as a function of the density parameter ρ_p . The physical dispersion relation is determined by intersecting the continuum of hypothetical dispersion relations with the frequency-dependent, effective density $\rho(f)$. The actual dispersion is determined implicitly by the relation $f = \tilde{f}(\mathbf{k}, \rho(f))$. By replacing the resonators with a uniform density medium, it is implicitly assumed that the dimensionless moment of inertia factor assumes the constant value of a rigid circular cylinder $I^A/[M^A(R^A)^2] = \frac{1}{2}$. In a physical resonator, the density is not spatially uniform. In extreme cases, the dimensionless moment of inertia factor could range from zero in the case of a point mass on the axis of rotation to unity when the mass is concentrated on the circular rim. However, as the resonant frequency of in-plane translation does not necessarily coincide with that of in-plane rotation, this leads to a fundamental incompatibility between the cutting surfaces defining the frequency-dependent effective mass and the moment of inertia. For example, over the frequency range of the third in-plane acoustic band, the effective moment of inertia is positive, while the effective mass is negative. It is impossible to consistently simulate positive moment of inertia and negative mass simultaneously in the CSM construction. In other words, the CSM is unable to describe the coupling between translational resonance of a unit and the rotational resonance of a neighboring unit at another location. This

underscores the necessity of our EIST formulation in Eq. (32) that allows a different, effective, frequency-dependent inertial parameter for each degree of freedom and couples them correctly through the wave-vector-dependent spring tensor.

V. EXAMPLE C: DOUBLE-CORE SINGLE-SHELL LOCAL RESONATORS

In order to illustrate the power of the EIST model in describing the modes of a medium with multiple, coupled, local resonances, we consider a resonator with more complex internal degrees of freedom. We study the acoustic band structure of a square lattice of right, circular steel cylinders, encapsulated by an inner, coaxial steel shell and an outer, coaxial cellulose, surrounded by open-cell foam. The internal degrees of freedom give rise to multiple resonances. The effective, frequency-dependent masses and moment of inertia each have two resonances. This illustrates the possibilities of designing flat acoustic bands using structures with two resonances that are close in resonant frequencies. The band structures determined by the appropriate EIST model agree, within 4.0%, with exact FEM results.

A. Model C

A square-lattice phononic crystal consisting of circular steel rods with lattice constant $a = 1 \text{ cm}$ is again considered. Each circular steel rod is coupled to a concentric steel core (inner shell) via open-cell foam. The resonator is encapsulated by a coaxial, circular, stiff cellulose outer shell. The background is the same type of open-cell foam. The inner steel core, inner annular foam region, concentric steel core, outer annular foam region, and cellulose shell fill $\phi_{c1}^C = 5\%$, $\phi_{f1}^C = 15\%$, $\phi_{c2}^C = 15\%$, $\phi_{f2}^C = 15\%$, and $\phi_s^C = 20\%$ by volume, respectively. The volume fraction of the exterior foam is $\phi_f^C = 30\%$. The radius of the inner circular steel rod is $R_1^C = a\sqrt{\phi_{c1}^C/\pi} \approx 0.1262 \text{ cm}$. The inner radius of the concentric steel core is $R_2^C = a\sqrt{(\phi_{c1}^C + \phi_{f1}^C)/\pi} \approx 0.2523 \text{ cm}$ and the outer radius is $R_3^C = a\sqrt{(\phi_{c1}^C + \phi_{f1}^C + \phi_{c2}^C)/\pi} \approx 0.3338 \text{ cm}$. The inner radius of the exterior cellulose shell is $R_4^C = a\sqrt{(\phi_{c1}^C + \phi_{f1}^C + \phi_{c2}^C + \phi_{f2}^C)/\pi} \approx 0.3989 \text{ cm}$, and the outer radius is $R_5^C = a\sqrt{(\phi_{c1}^C + \phi_{f1}^C + \phi_{c2}^C + \phi_{f2}^C + \phi_s^C)/\pi} \approx 0.4720 \text{ cm}$. The unit cell is depicted in Fig. 10. The filling fractions are chosen to retain the same overall proportions of steel, cellulose, and foam in a unit cell as model B, at 20%, 20%, and 60%, respectively.

The stiff cores and shell are approximated as rigid bodies with four mechanical degrees of freedom each. The inner steel core displaces in plane in the x/y direction by X_{c1}^C/Y_{c1}^C , displaces out of plane in the z direction by Z_c^C , and rotates counterclockwise by Ψ_{c1}^C , from the equilibrium position. The corresponding dynamical variables of the annular steel core and the cellulose shell are $(X_{c2}^C, Y_{c2}^C, Z_{c2}^C, \Psi_{c2}^C)$ and $(X_s^C, Y_s^C, Z_s^C, \Psi_s^C)$, respectively. The mass per unit length of the inner steel core M_{c1}^C , the annular steel core M_{c2}^C , and the cellulose shell M_s^C are given by

$$M_{c1}^C = \rho_c \pi (R_1^C)^2 \approx 0.0397 \text{ kg m}^{-1}, \quad (34a)$$

$$M_{c2}^C = \rho_c \pi [(R_3^C)^2 - (R_2^C)^2] \approx 0.1191 \text{ kg m}^{-1}, \quad (34b)$$

$$M_s^C = \rho_s \pi [(R_5^C)^2 - (R_4^C)^2] \approx 0.02700 \text{ kg m}^{-1}. \quad (34c)$$

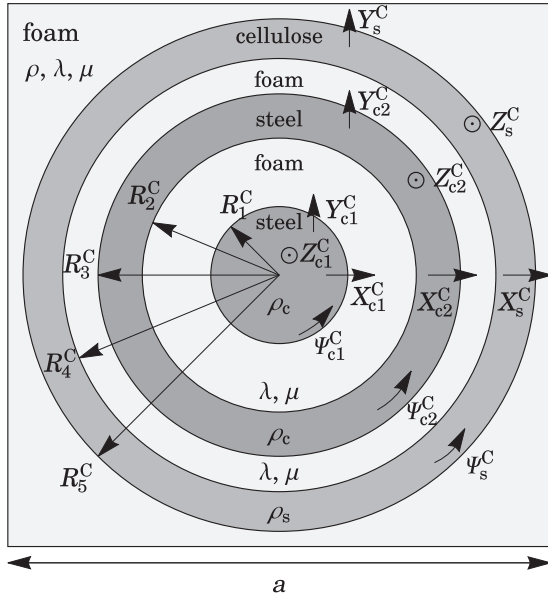


FIG. 10. A unit cell in model C consists of a square lattice of dense steel rods of radius $R_1^C \approx 0.1262$ cm, each surrounded by another concentric, circular steel core of inner radius $R_2^C \approx 0.2523$ cm and outer radius $R_3^C \approx 0.3338$ cm. The resonator is encapsulated by an concentric coaxial annular cellulose shell of inner radius $R_4^C \approx 0.3989$ cm and outer radius $R_5^C \approx 0.4720$ cm. The interstitial spaces are filled with open-cell foam. The lattice constant is $a = 1$ cm. The unit cell is described by 12 mechanical degrees of freedom, including the translation in the $x/y/z$ direction $X_{c1}^C/Y_{c1}^C/Z_{c1}^C$ and axial rotation Ψ_{c1}^C of the interior steel core, as well as the corresponding variables $X_{c2}^C, Y_{c2}^C, Z_{c2}^C$, and Ψ_{c2}^C of the concentric annular steel core. X_s^C, Y_s^C, Z_s^C , and Ψ_s^C are those of the outermost cellulose shell.

Similarly, the moment of inertia per unit length of the interior steel core I_{c1}^C , annular steel core I_{c2}^C , and the cellulose shell I_s^C are given by

$$I_{c1}^C = \frac{\pi}{2} \rho_c (R_1^C)^4 \approx 0.03159 \times 10^{-6} \text{ kg m}, \quad (35a)$$

$$I_{c2}^C = \frac{\pi}{2} \rho_c [(R_3^C)^4 - (R_2^C)^4] \approx 1.043 \times 10^{-6} \text{ kg m}, \quad (35b)$$

$$I_s^C = \frac{\pi}{2} \rho_s [(R_5^C)^4 - (R_4^C)^4] \approx 0.5157 \times 10^{-6} \text{ kg m}. \quad (35c)$$

The equations of motion are given by

$$M_{c1}^C \ddot{X}_{c1}^C = F_{c,x}^C, \quad (36a)$$

$$M_{c2}^C \ddot{X}_{c2}^C = -F_{c,x}^C - F_{s,x}^C, \quad (36b)$$

$$M_s^C \ddot{X}_s^C = F_{s,x}^C + F_{b,x}^C, \quad (36c)$$

$$M_{c1}^C \ddot{Y}_{c1}^C = F_{c,y}^C, \quad (36d)$$

$$M_{c2}^C \ddot{Y}_{c2}^C = -F_{c,y}^C - F_{s,y}^C, \quad (36e)$$

$$M_s^C \ddot{Y}_s^C = F_{s,y}^C + F_{b,y}^C, \quad (36f)$$

$$M_{c1}^C \ddot{Z}_{c1}^C = F_{c,z}^C, \quad (36g)$$

$$M_{c2}^C \ddot{Z}_{c2}^C = -F_{c,z}^C - F_{s,z}^C, \quad (36h)$$

$$M_s^C \ddot{Z}_s^C = F_{s,z}^C + F_{b,z}^C, \quad (36i)$$

$$I_{c1}^C \ddot{\Psi}_{c1}^C = \tau_c^C, \quad (36j)$$

$$I_{c2}^C \ddot{\Psi}_{c2}^C = -\tau_c^C - \tau_s^C, \quad (36k)$$

$$I_s^C \ddot{\Psi}_s^C = \tau_s^C + \tau_b. \quad (36l)$$

Here, $\mathbf{F}_{c/s}^C = F_{c/s,x}^C \hat{\mathbf{x}} + F_{c/s,y}^C \hat{\mathbf{y}} + F_{c/s,z}^C \hat{\mathbf{z}}$ and $\tau_{c/s}^C = \tau_{c/s}^C \hat{\mathbf{z}}$ denote the force and the torque per unit length acting on the interior steel core and cellulose shell by the interstitial foam, respectively. Under the rigid core-shell approximations (RCSA), the regions of the interstitial foam satisfy elastostatic equilibrium under appropriate boundary conditions specified by (angular) displacement of the rigid bodies [9,23]. The elastic restoring forces due to the foam assume the form of Hooke's law:

$$F_{c,x}^C = k_{x1}^C (X_{c1}^C - X_{c1}^C), \quad (37a)$$

$$F_{s,x}^C = k_{x2}^C (X_{c2}^C - X_s^C), \quad (37b)$$

$$F_{c,y}^C = k_{y1}^C (Y_{c2}^C - Y_{c1}^C), \quad (37c)$$

$$F_{s,y}^C = k_{y2}^C (Y_{c2}^C - Y_s^C), \quad (37d)$$

$$F_{c,z}^C = k_{z1}^C (Z_{c2}^C - Z_{c1}^C), \quad (37e)$$

$$F_{s,z}^C = k_{z2}^C (Z_{c2}^C - Z_s^C), \quad (37f)$$

$$\tau_c^C = k_{\psi 1}^C (\Psi_{c2}^C - \Psi_{c1}^C), \quad (37g)$$

$$\tau_s^C = k_{\psi 2}^C (\Psi_{c2}^C - \Psi_s^C), \quad (37h)$$

where the spring constants depend on the geometry and the Lamé parameter (λ, μ) of the foam [9]:

$$\begin{aligned} k_{x1}^C &= k_{y1}^C = 4\pi\mu(\lambda + 2\mu)(\lambda + 3\mu)[(R_1^C)^2 + (R_2^C)^2] / \\ &\quad \{(\lambda + 3\mu)^2[(R_1^C)^2 + (R_2^C)^2] \ln R_2^C/R_1^C \\ &\quad - (\lambda + \mu)^2[(R_2^C)^2 - (R_1^C)^2]\} \\ &\approx 2.960 \times 10^5 \text{ N m}^{-2}, \end{aligned} \quad (38a)$$

$$\begin{aligned} k_{x2}^C &= k_{y2}^C = 4\pi\mu(\lambda + 2\mu)(\lambda + 3\mu)[(R_3^C)^2 + (R_4^C)^2] / \\ &\quad \{(\lambda + 3\mu)^2[(R_3^C)^2 + (R_4^C)^2] \ln R_4^C/R_3^C \\ &\quad - (\lambda + \mu)^2[(R_4^C)^2 - (R_3^C)^2]\} \\ &\approx 1.214 \times 10^6 \text{ N m}^{-2}, \end{aligned} \quad (38b)$$

$$k_{z1}^C = \frac{2\pi\mu}{\ln R_2^C/R_1^C} \approx 1.394 \times 10^6 \text{ N m}^{-2}, \quad (38c)$$

$$k_{z2}^C = \frac{2\pi\mu}{\ln R_4^C/R_3^C} \approx 5.419 \times 10^6 \text{ N m}^{-2}, \quad (38d)$$

$$k_{\psi 1}^C = \frac{4\pi\mu(R_1^C)^2(R_2^C)^2}{(R_2^C)^2 - (R_1^C)^2} \approx 0.4101 \text{ N}, \quad (38e)$$

$$k_{\psi 2}^C = \frac{4\pi\mu(R_3^C)^2(R_4^C)^2}{(R_4^C)^2 - (R_3^C)^2} \approx 7.177 \text{ N}. \quad (38f)$$

B. Two-resonance effective mass

The equations of motion of the in-plane rotation and translations in three orthogonal directions can again be mapped to a set of frequency-dependent effective inertias. The treatment

parallels the single-resonance mass-in-a-box case introduced in Sec. IV B. A rigid box of mass m_s with displacement x_s , which responds to an external harmonic force $F(f)$, contains a box of mass m_{c2} with displacement x_{c2} held by a spring with stiffness constant k_2 . The interior box m_{c2} contains a massive core m_{c1} with displacement x_{c1} , connected by a spring with stiffness constant k_1 . This response is governed by the equations of motion

$$m_{c1}\ddot{x}_{c1} = k_1(x_{c2} - x_{c1}), \quad (39a)$$

$$m_{c2}\ddot{x}_{c2} = k_1(x_{c1} - x_{c2}) + k_2(x_s - x_{c2}), \quad (39b)$$

$$m_s\ddot{x}_s = F(f) + k(x_{c2} - x_s). \quad (39c)$$

Under the external harmonic force, all masses oscillate at the same frequency f . A straightforward method to obtain an effective mass description of the resonator is to calculate the frequency-dependent proportionality factors between the displacements by solving the linear system. An alternative approach relies on successive applications of Eq. (25). The interior masses m_{c1} and m_{c2} are recognized as a single-resonance oscillator with an effective, frequency-dependent mass $m_{c2,e}(f)$:

$$m_{c2,e}(f) = m_{c2} + \frac{m_{c1}k_1}{k_1 - 4\pi^2 f^2 m_{c1}}. \quad (40)$$

The outermost rigid box m_s is coupled to a locally resonant core. The frequency-independent mass m_2 of the core in (25) is replaced by the frequency-dependent mass $m_{c2,e}(f)$. Hence, the entire resonator has an effective mass $m_{s,e}(f)$:

$$m_{s,e}(f) = m_s + \frac{m_{c2,e}(f)k_2}{k_2 - 4\pi^2 f^2 m_{c2,e}(f)}. \quad (41)$$

$m_{s,e}(f)$ is a rational function in f^2 , with quadratic dependencies on f^2 in both the numerator and the denominator. The zeros of the denominator are the resonant frequencies $f_{0,\pm}$ at which the effective mass diverges. The zeros of the numerator are the zero-mass frequencies $f_{*,\pm}$ where the effective mass changes its sign:

$$f_{0,\pm} = \frac{1}{2\pi} \left\{ \frac{k_1 + k_2}{2m_{c2}} + \frac{k_1}{2m_{c1}} \pm \left[\left(\frac{k_1 + k_2}{2m_{c2}} + \frac{k_1}{2m_{c1}} \right)^2 - \frac{k_1 k_2}{m_{c1} m_{c2}} \right]^{1/2} \right\}^{1/2}, \quad (42)$$

$$f_{*,\pm} = \frac{1}{2\pi} \left\{ \frac{k_1}{2m_{r1}} + \frac{k_2}{2m_{r2}} \pm \left[\left(\frac{k_1}{2m_{r1}} + \frac{k_2}{2m_{r2}} \right)^2 - \frac{k_1 k_2 (m_{c1} + m_{c2} + m_s)}{m_{c1} m_{c2} m_s} \right]^{1/2} \right\}^{1/2}, \quad (43)$$

where $m_{r1} = m_{c1}m_{c2}/(m_{c1} + m_{c2})$ and $m_{r2} = m_{c2}m_s/(m_{c2} + m_s)$ are reduced masses. We rewrite the effective mass $m_{s,e}(f)$ in a compact form using its characteristic frequencies:

$$m_{s,e}(f) = m_s \left[\frac{(f_{*,+}^2 - f^2)(f_{*,-}^2 - f^2)}{(f_{0,+}^2 - f^2)(f_{0,-}^2 - f^2)} \right]. \quad (44)$$

This is plotted as a function of frequency in Fig. 11. The effective mass increases from the total mass of the system at zero frequency to infinity at the first resonant frequency

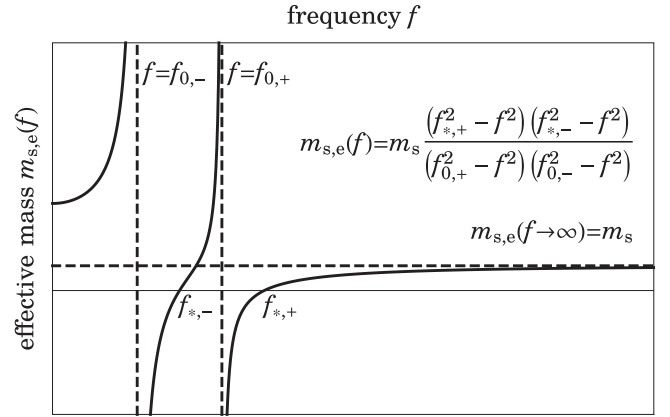


FIG. 11. Nondissipative, frequency-dependent effective mass in Eq. (44) is schematically plotted. Note that the effective mass diverges at $f = f_{0,\pm}$, and is negative over the ranges $f_{0,-} < f < f_{*,-}$ and $f_{0,+} < f < f_{*,+}$.

$f_{0,-}$. Over the frequency range $f_{0,-} < f < f_{*,-}$, the effective mass is negative, and wave propagation is inhibited over such frequency range. The effective mass changes its sign and increases from zero at $f = f_{*,-}$ to infinity at the second resonant frequency $f = f_{0,+}$. Over the frequency range $f_{0,+} < f < f_{*,+}$, the effective mass is, again, negative, and wave propagation is inhibited. Beyond that, the effective mass increases from zero at $f = f_{*,+}$ to the mass of the outermost box in the high-frequency limit.

Under the RCSA, the two layers of interstitial foam act as Hookean springs, and the coupled equations of motion in (36a)–(36l) are mapped to two-resonance models in (39a)–(39c). The resonant unit is described by the frequency-dependent, effective masses $M_{x,e}^C(f)$ and $M_{y,e}^C(f)$ for in-plane translations, effective mass $M_{z,e}^C(f)$ for out-of-plane translation, and the effective moment of inertia $I_e^C(f)$ for in-plane rotation:

$$M_{x,e}^C(f) = M_{y,e}^C(f) = M_s^C \left[\frac{(f_{*+,t}^C{}^2 - f^2)(f_{*-,t}^C{}^2 - f^2)}{(f_{0+,t}^C{}^2 - f^2)(f_{0-,t}^C{}^2 - f^2)} \right], \quad (45a)$$

$$M_{z,e}^C(f) = M_s^C \left[\frac{(f_{*+,z}^C{}^2 - f^2)(f_{*-,z}^C{}^2 - f^2)}{(f_{0+,z}^C{}^2 - f^2)(f_{0-,z}^C{}^2 - f^2)} \right], \quad (45b)$$

$$I_e^C(f) = I_s^C \left[\frac{(f_{*+,r}^C{}^2 - f^2)(f_{*-,r}^C{}^2 - f^2)}{(f_{0+,r}^C{}^2 - f^2)(f_{0-,r}^C{}^2 - f^2)} \right]. \quad (45c)$$

Here, the resonant frequencies of in-plane translation $f_{0-,t}^C \approx 357.0$ Hz, $f_{0+,t}^C \approx 618.5$ Hz, out-of-plane translation $f_{0-,z}^C \approx 241.8$ Hz, $f_{0+,z}^C \approx 418.8$ Hz and in-plane rotation $f_{0-,r}^C \approx 405.5$ Hz, $f_{0+,r}^C \approx 590.6$ Hz are determined by Eqs. (34a)–(35c), (38a)–(38f), and (42). Similarly, the zero-effective density frequencies for in-plane translation $f_{*-,t}^C \approx 487.7$ Hz, $f_{*+,t}^C \approx 1187.9$ Hz, out-of-plane translation $f_{*-,z}^C \approx 334.6$ Hz, $f_{*+,z}^C \approx 793.9$ Hz, and in-plane rotation $f_{*-,r}^C \approx 574.4$ Hz, $f_{*+,r}^C \approx 732.0$ Hz are determined by Eqs. (34a)–(35c), (38a)–(38f), and (43).

C. Acoustic band structure in the EIST model

As the shell of the resonators is significantly stiffer than the open-cell foam background, the outermost shell retains its circular shape at the frequencies of interest. The translation and rotation of the rigid cellulose shell determine the boundary conditions of the foam background. Since the steel-core resonators in model C occupy the same volume as the cellulose cylinders in model A, embedded in the same type of background foam, we apply the same background spring tensor. By the equations of motion (36g)–(36i) and the effective mass (45b), the out-of-plane oscillation frequencies are governed by

$$4\pi^2 M_{z,e}^C(f) f^2 = k_{zz}(\mathbf{K}). \quad (46)$$

This is a cubic equation in f^2 .

The first three out-of-plane acoustic bands are plotted in Fig. 12. At a given wave vector \mathbf{K} , the left-hand side in Eq. (46) intersects the non-negative background spring constant $k_{zz}(\mathbf{K})$ exactly three times. The first intersection occurs over $0 \leq f < f_{0-,z}$, as it increases from zero at $f = 0$ to infinity at the first resonant frequency $f = f_{0-,z}$. The second intersection occurs over $f_{*-z} \leq f < f_{0+,z}$, as the effective mass increases from zero at $f = f_{*-z}$ to infinity at the second resonant frequency $f = f_{0+,z}$. The third intersection occurs over $f_{*+,z} \leq f$ when the left-hand side in Eq. (46) increases monotonically without bound from zero at $f = f_{*+,z}$. When the effective mass is negative over the frequency ranges $f_{0-,z} < f < f_{*-z}$ and $f_{0+,z} < f < f_{*+,z}$, the left-hand side

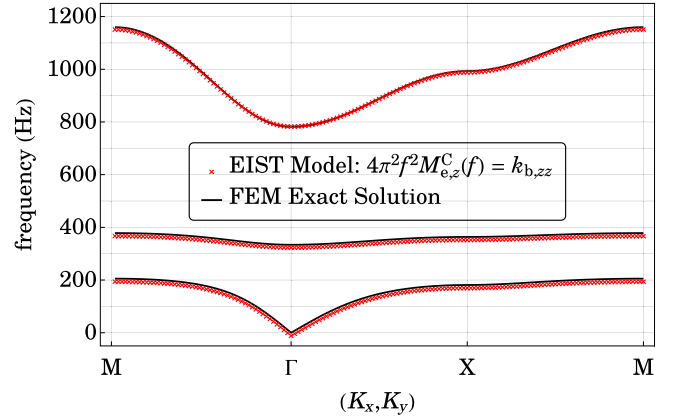


FIG. 12. The first three out-of-plane acoustic bands of the periodic, locally resonant double-core steel-cellulose-foam composite (model C) are plotted in the first Brillouin zone along the path $M \rightarrow \Gamma \rightarrow X \rightarrow M$ for the EIST model in Eq. (46) (red crosses). The finite-element method (solid black line) is used to calculate the exact out-of-plane bands of the actual phononic crystal. The maximum percentage error is 1.6%.

in Eq. (46) is negative and does not intersect with the non-negative background spring constant $k_{zz}(\mathbf{K})$. These spectral regions correspond to acoustic band gaps, whereas the number of positive branches of the effective mass is equal to the number of low-frequency acoustic bands.

The in-plane oscillation frequencies involve solving a degree-nine polynomial equation in f^2 :

$$\det \begin{pmatrix} k_{xx}(\mathbf{K}) - 4\pi^2 f^2 M_{x,e}^C(f) & k_{xy}(\mathbf{K}) & k_{x\psi}(\mathbf{K}) \\ k_{yx}(\mathbf{K}) & k_{yy}(\mathbf{K}) - 4\pi^2 f^2 M_{y,e}^C(f) & k_{y\psi}(\mathbf{K}) \\ k_{\psi x}(\mathbf{K}) & k_{\psi y}(\mathbf{K}) & k_{\psi\psi}(\mathbf{K}) - 4\pi^2 f^2 I_e^C(f) \end{pmatrix} = 0. \quad (47)$$

These in-plane acoustic bands are plotted in Fig. 13. The frequency-dependent, effective masses for in-plane translation and moment of inertia for in-plane rotation each contains three positive branches. The three in-plane bands in the nonresonant case (model A) are split into nine planar bands. There are disjoint band gaps for $343.3 \text{ Hz} < f < 486.7 \text{ Hz}$ and $585.0 \text{ Hz} < f < 877.7 \text{ Hz}$. These correspond to the frequency ranges where the effective masses for in-plane translation and moment of inertia for in-plane rotation are simultaneously negative.

Clearly, our EIST model provides accurate and reliable acoustic band structure for complex systems with multiple resonances. A striking feature is the occurrence of several very flat bands occurring over a narrow frequency range $f_{*,-} < f < f_{0,+}$, between acoustic band gaps. In photonics, flat photonic bands enable slow-light modes and refraction almost parallel to the interface of incidence. This has applications in thin-film solar energy harvesting [25,26]. It is plausible that efficient, thin-film sound-absorbing devices can be likewise designed utilizing the slow-sound, flat acoustic bands.

VI. DISCUSSION

In the EIST model, the local resonances are recaptured with the frequency-dependent, effective inertial parameters, while periodicity effects are contained in the spring tensor. This suggests the possibility of generalizing the EIST model to describe some features of disordered systems where the positions of the resonators are randomized. One form of disorder consists of spatially varying orientations of the square lattice. This leads to random scattering of acoustic waves and the true modes involve a superposition of the wave vector \mathbf{K} over a range proportional to $1/l_{\text{scatt}}$, where l_{scatt} is the scattering mean-free path.

An orientationally disordered medium could be represented by averaging the spring tensor components over some range of angles of the Bloch wave vector. If full angular averages are taken for all the spring tensor components, the four degrees of freedom are decoupled since only the diagonal components have nonvanishing angular averages. Using the resonant units in example B, the out-of-plane and in-plane acoustic band structures of a hypothetical medium with spring

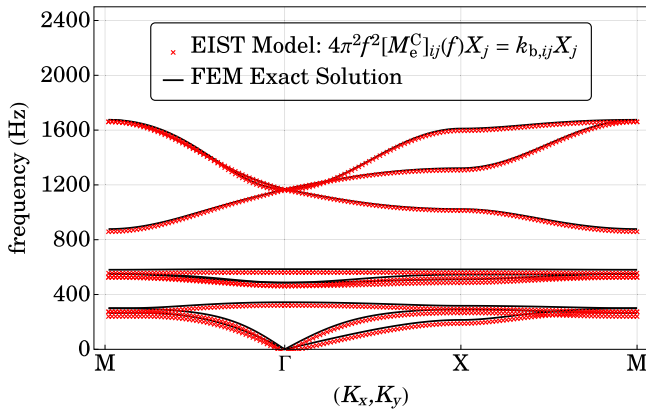


FIG. 13. The first nine in-plane acoustic bands of the periodic, locally resonant double-core steel-cellulose-foam composite (model C) are plotted in the first Brillouin zone along the path $M \rightarrow \Gamma \rightarrow X \rightarrow M$ for the EIST model in Eq. (47) (red crosses). The finite-element method (solid black line) is used to calculate the in-plane bands of the exact phononic crystal. The maximum relative error is 4.0%.

tensor averaged over all orientations of the wave vector \mathbf{K} are plotted in Figs. 14 and 15, respectively.

The acoustic band gaps of this averaged medium agree with those of the periodic structure, confirming that the low-frequency band gaps are caused by local resonances rather than spatial periodicity. It also suggests that locally resonant media without strict periodicity can be modeled by suitable modifications or simplifications of the spring tensor.

A slightly disordered medium might be represented by a modified spring tensor using the circular harmonic expansion in the orientation angle of the wave vector \mathbf{K} . A simple representation that retains coupling between the different degrees of freedom is when the Fourier series of each

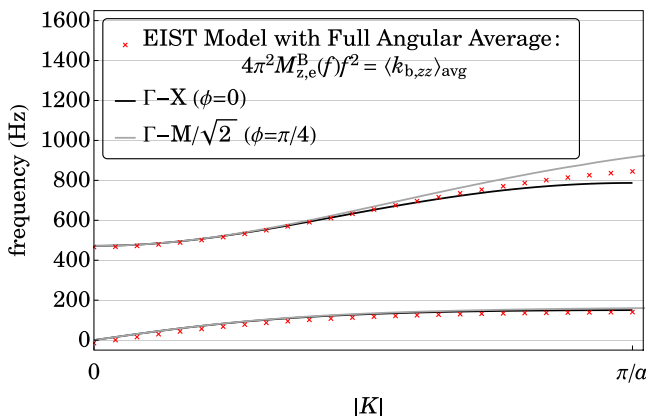


FIG. 14. The first two out-of-plane acoustic bands of the locally resonant core-shell unit (model B) for a completely angle-averaged spring tensor (red crosses) are plotted from the center of the first Brillouin zone to the radius of the largest inscribed circle at $K = \pi/a$. $\langle k_{b,zz} \rangle_{avg}$ denotes the completely angular-averaged out-of-plane spring tensor component $k_{b,zz}$. For comparison, the bands of the periodic medium are plotted along $\Gamma - X$ where $\phi = 0$ (black solid line) and along $\Gamma - M/\sqrt{2}$ where $\phi = \pi/4$ (gray solid line).

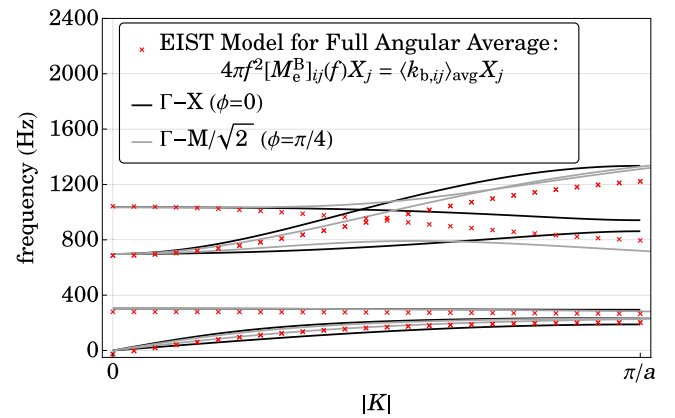


FIG. 15. The first six in-plane acoustic bands of the locally resonant core-shell unit (model B) in a completely angle-averaged spring tensor (red crosses) are plotted from the center of the first Brillouin zone to the radius of the largest inscribed circle at $K = \pi/a$. $\langle k_{ij} \rangle_{avg}$ denotes the in-plane spring tensor component k_{ij} completely averaged over the orientation of the wave vector. For comparison, the bands of the periodic medium are plotted along $\Gamma - X$ where $\phi = 0$ (black solid line) and along $\Gamma - M/\sqrt{2}$ where $\phi = \pi/4$ (gray solid line). The in-plane translational modes are degenerate for the fully angular-averaged spring tensor.

spring tensor component is truncated at the leading nonzero angle-dependent term. With the resonant units in example B, the out-of-plane and in-plane acoustic band structures of this hypothetical partially disordered medium are plotted in Figs. 16 and 17, respectively. The acoustic band gaps of the simplified system again coincide with those of the exact periodic structure. The first two out-of-plane acoustic bands are insensitive to this reduction of the spring tensor implied by slight disorder. On the other hand, the in-plane acoustic bands are increasingly sensitive to the slight disorder at higher frequencies and larger wave vectors. A more detailed description

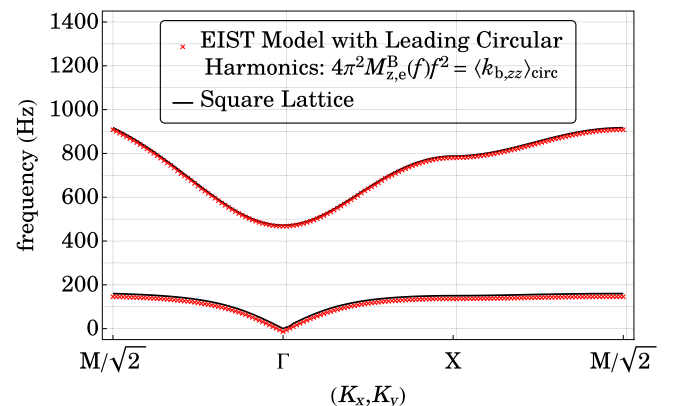


FIG. 16. The first two out-of-plane acoustic bands of the locally resonant core-shell unit (model B) for a leading circular harmonic spring tensor representation (red crosses) are plotted along a circular sector in the first Brillouin zone $M/\sqrt{2} \rightarrow \Gamma \rightarrow X \rightarrow M/\sqrt{2}$. $\langle k_{b,zz} \rangle_{circ}$ denotes the leading circular harmonic approximation of the out-of-plane spring tensor component $k_{b,zz}$. For comparison, the bands of the periodic medium (black solid line) are plotted along the same path.

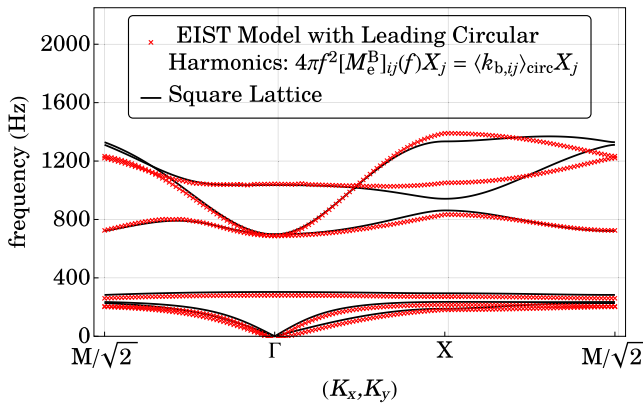


FIG. 17. The first six out-of-plane acoustic bands of the locally resonant core-shell unit (model B) in a leading circular harmonic spring tensor representation (red crosses) are plotted along a circular sector in the first Brillouin zone $M/\sqrt{2} \rightarrow \Gamma \rightarrow X \rightarrow M/\sqrt{2}$. $\langle k_{ij} \rangle_{\text{circ}}$ denotes the leading circular harmonic approximation of the spring tensor component k_{ij} . For comparison, the bands of the periodic medium (black solid line) are plotted along the same path. Modes at higher frequencies and wavevectors are more sensitive to the slight disorder.

would require an ensemble of different spring tensors obeying a suitable probability distribution, rather than just a single average value of the spring tensor.

Our EIST model can also be easily generalized to three-dimensional, locally resonant acoustic materials. For a spherical resonator shell, the internal elastic deformation analysis and the external spring tensor evaluation are facilitated by spherical harmonics $Y_{l,m}(\theta, \phi)$ and spherical Bessel function $j_n(\omega r/c_{l,t})$ expansions, rather than their cylindrical counterparts. Here, $c_l = \sqrt{(\lambda + 2\mu)/\rho}$ and $c_t = \sqrt{\mu/\rho}$ denote the longitudinal and transverse speeds of sound in an isotropic, linear elastic medium, respectively. If the resonator is encapsulated by a rigid shell, translations and rotations in three orthogonal directions are the six degrees of freedom that couple to the elastic background. When the acoustic wavelength is much longer than the length scales of a three-dimensional resonator, the internal deformation can be described by elastostatic equilibrium conditions. Inside the spherical resonator, the shear and compressional potentials (see Appendix B) are expressible as the solution of the Laplace equation in spherical coordinates. The potential functions can be used to calculate the displacement profile inside the resonator, and thus the elastic stress, force, and torque acting on the exterior shell. These yield the frequency-dependent, effective masses and moments of inertia, corresponding to the translational and rotational oscillations of the resonator in three orthogonal directions, respectively. Similar to the two-dimensional cases, the inertial parameters are rational functions of frequency squared, with the zeros of the denominator associated with the resonant frequencies. The coupling between the spherical resonators can be described by a 6×6 wave-vector-dependent spring tensor. In the background, a full wave treatment is necessary. It is possible to calculate the spring tensor via plane-wave expansion by replacing the spherical resonator by a nonresonant stiff sphere. An alternative approach involves partial-wave analysis

and multiple scattering of the elastic potentials in the basis of spherical waves.

In the physical models we studied, translations in three orthogonal directions and axial rotation are the predominant degrees of freedom of the shell that couple to the background foam at low frequencies below 1000 Hz. Modes involving deformation of the shell occur beyond 3000 Hz. The accuracy of the EIST model declines, if the effective mass and the effective moment of inertia of the resonator are sufficiently small, to an extent that the frequencies of the translational and rotational modes are comparable to those involving elastic deformations of the shell. In that case, additional degrees of freedom associated with the deformation of the resonator shell are necessary to recapture the acoustic wave spectrum. Another source of error arises from the elastostatic approximation leading to the frequency-dependent, effective inertial parameters. The interstitial foam in models B and C is approximated as linear, massless springs. The restoring forces and torques are determined under an elastostatic equilibrium. When the wavelength is comparable to the size of the resonator at sufficiently high frequencies, wavelike properties in the interstitial foam cannot be ignored. A more precise treatment of the internal resonances will be necessary.

Our methodology can also be applied to structures with other types of oscillatory responses. Consider a resonator with a softer elastic shell that responds to monopolar compressional oscillations. It is possible to associate the volume change as a degree of freedom, and relate the underlying generalized inertial parameter to the effective bulk modulus. Internal degrees of freedom that couple to the compressional mode can be absorbed in the frequency dependence of the effective bulk modulus. The spring tensor can be extended to incorporate the coupling of the compressional mode and other degrees of freedom of spatially separated resonators.

We hope that the examples we have presented reveal the power and precision of our effective inertia and spring tensor construction describing locally resonant acoustic materials. We expect that a number of generalizations to more complex systems will ensue.

ACKNOWLEDGMENT

This work was supported in part by the Natural Sciences and Engineering Research Council of Canada.

APPENDIX A: BACKGROUND SPRING TENSOR BY PLANE-WAVE EXPANSION

The spring tensor is evaluated via plane-wave expansion. The associated matrices are theoretically infinite in size. They are truncated with 31 plane waves per direction to recapture the finite-element method (FEM) results. Under such plane-wave truncation, $(31)^2 = 961$ plane waves are incorporated.

Bloch's theorem states that acoustic waves in a periodic medium can be expressed as a plane wave modulated by a function with the periodicity of the crystal:

$$\mathbf{u}(\mathbf{r}, t) = \exp(i\mathbf{K} \cdot \mathbf{r} - i\omega\mathbf{K}t) \sum_{\mathbf{G}} \mathbf{u}_{\mathbf{K}}(\mathbf{G}) \exp(i\mathbf{G} \cdot \mathbf{r}). \quad (\text{A1})$$

Here, \mathbf{K} denotes the Bloch wave vector, \mathbf{G} denotes a reciprocal lattice vector, $\mathbf{u}_{\mathbf{K}}(\mathbf{G})$ denotes the Fourier coefficient of the underlying periodic function, and $\omega_{\mathbf{K}}$ denotes the angular frequency. When the density and elastic parameters are decomposed into Fourier series, algebraic eigenvalue equations are obtained from the dynamical equations (5), (6a), and (6b) [see Eqs. (A8) and (A9) in [9]]. The dispersion relation $\omega_{\mathbf{K}}$ describes the acoustic band structure.

Similarly, the stress tensor can be decomposed into Bloch waves:

$$\sigma_{pq}(\mathbf{r}, t) = \exp(i\mathbf{K} \cdot \mathbf{r} - i\omega_{\mathbf{K}}t) \sum_{\mathbf{G}} \sigma_{pq}(\mathbf{G}) \exp(i\mathbf{G} \cdot \mathbf{r}), \quad (\text{A2})$$

where $\sigma_{pq}(\mathbf{G})$ denotes the Fourier coefficient of the periodic function associated with the stress tensor. The contraction of the elasticity tensor C_{ijkl} and the strain tensor ϵ_{kl} gives the stress tensor σ_{ij} . Fourier products with complementary discontinuities are treated by the ‘‘inverse rule’’ to ensure numerical convergence [9,27–29]:

$$\sigma_{pq}(\mathbf{G}) = \sum_{\mathbf{G}'} \left[\frac{1}{C_{pqrs}} \right]^{-1}(\mathbf{G}, \mathbf{G}') \left[\frac{1}{2}(iK_s + iG'_s)u_{r,\mathbf{K}}(\mathbf{G}') + \frac{1}{2}(iK_r + iG'_r)u_{s,\mathbf{K}}(\mathbf{G}') \right]. \quad (\text{A3})$$

The matrix element of $[1/C_{pqrs}]$ is $[1/C_{pqrs}](\mathbf{G}, \mathbf{G}') = (1/C_{pqrs})(\mathbf{G} - \mathbf{G}')$, where $(1/C_{pqrs})(\mathbf{G})$ denotes the Fourier coefficient of the reciprocal of the periodic, nonzero, elasticity tensor component. The superscript -1 denotes matrix inversion. Readers can refer to Appendix A in [9] and references therein for further discussion of the inverse rule to obtain uniform convergence across material discontinuity.

In two-dimensional, linear, isotropic elastic solids, the out-of-plane displacement field is decoupled from the in-plane displacement field. Spatial derivative with respect to z is null by translational symmetry ($\partial/\partial z = 0$). The elastic force acting on the cellulose shell involves the following components of the symmetric stress tensor:

$$\sigma_{xx}(\mathbf{G}) = \sum_{\mathbf{G}'} N_{\mathbf{G},\mathbf{G}'}^{\text{inv}} u_{x,\mathbf{K}}(\mathbf{G}') (iK_x + iG'_x) + \Lambda_{\mathbf{G},\mathbf{G}'}^{\text{inv}} u_{y,\mathbf{K}}(\mathbf{G}') (iK_y + iG'_y), \quad (\text{A4a})$$

$$\sigma_{xy}(\mathbf{G}) = \sigma_{yx}(\mathbf{G}) = \sum_{\mathbf{G}'} M_{\mathbf{G},\mathbf{G}'}^{\text{inv}} [u_{x,\mathbf{K}}(\mathbf{G}') (iK_y + iG'_y) + u_{y,\mathbf{K}}(\mathbf{G}') (iK_x + iG'_x)], \quad (\text{A4b})$$

$$\sigma_{yy}(\mathbf{G}) = \sum_{\mathbf{G}'} \Lambda_{\mathbf{G},\mathbf{G}'}^{\text{inv}} u_{x,\mathbf{K}}(\mathbf{G}') (iK_x + iG'_x) + N_{\mathbf{G},\mathbf{G}'}^{\text{inv}} u_{y,\mathbf{K}}(\mathbf{G}') (iK_y + iG'_y), \quad (\text{A4c})$$

$$\sigma_{zx}(\mathbf{G}) = \sigma_{xz}(\mathbf{G}) = \sum_{\mathbf{G}'} M_{\mathbf{G},\mathbf{G}'}^{\text{inv}} u_{z,\mathbf{K}}(\mathbf{G}') (iK_x + iG'_x), \quad (\text{A4d})$$

$$\sigma_{zy}(\mathbf{G}) = \sigma_{yz}(\mathbf{G}) = \sum_{\mathbf{G}'} M_{\mathbf{G},\mathbf{G}'}^{\text{inv}} u_{z,\mathbf{K}}(\mathbf{G}') (iK_y + iG'_y). \quad (\text{A4e})$$

In our two-dimensional elastic composite consisting of linear isotropic materials, the relevant nonvanishing components are $C_{1122} = C_{2211} = \lambda$, $C_{1212} = C_{2121} = C_{3131} = C_{3232} = 2\mu$,

$C_{1111} = C_{2222} = \lambda + 2\mu$. For notational convenience, the matrices $\Lambda_{\mathbf{G},\mathbf{G}'}^{\text{inv}}$, $M_{\mathbf{G},\mathbf{G}'}^{\text{inv}}$, and $N_{\mathbf{G},\mathbf{G}'}^{\text{inv}}$ are introduced, with their elements defined by

$$M_{\mathbf{G},\mathbf{G}'}^{\text{inv}} = \frac{1}{2} \left[\frac{1}{C_{1212}} \right]^{-1}(\mathbf{G}, \mathbf{G}'), \quad (\text{A5a})$$

$$\Lambda_{\mathbf{G},\mathbf{G}'}^{\text{inv}} = \left[\frac{1}{C_{1122}} \right]^{-1}(\mathbf{G}, \mathbf{G}'), \quad (\text{A5b})$$

$$N_{\mathbf{G},\mathbf{G}'}^{\text{inv}} = \left[\frac{1}{C_{1111}} \right]^{-1}(\mathbf{G}, \mathbf{G}'). \quad (\text{A5c})$$

The elastic restoring force and torque acting on the shell due to the background are given by the following integrals:

$$\begin{aligned} F_{b,i}(\mathbf{K}) &= \oint_{\{s=R_1^A\}} dl (\sigma_{ix} \cos \phi + \sigma_{iy} \sin \phi) \\ &= 2\pi i R_1^A \sum_{\mathbf{G}} [\sigma_{ix}(\mathbf{G})(K_x + G_x) + \sigma_{iy}(\mathbf{G})(K_y + G_y)] \\ &\quad \times \frac{J_1(|\mathbf{K} + \mathbf{G}| R_1^A)}{|\mathbf{K} + \mathbf{G}|} e^{-i\omega_{\mathbf{K}}t}, \end{aligned} \quad (\text{A6a})$$

$$\begin{aligned} \tau_{b,\psi}(\mathbf{K}) &= \oint_{\{s=R_1^A\}} dl \hat{\mathbf{z}} \cdot [\mathbf{r} \times (\boldsymbol{\sigma} \cdot \hat{\mathbf{s}})] \\ &= \oint_{\{s=R_1^A\}} dl R_1^A \left[\sigma_{xy} \cos 2\phi + \frac{1}{2}(\sigma_{yy} - \sigma_{xx}) \sin 2\phi \right] \\ &= -2\pi (R_1^A)^2 \sum_{\mathbf{G}} \{ \sigma_{xy}(\mathbf{G}) [(K_x + G_x)^2 - (K_y + G_y)^2] \\ &\quad + [\sigma_{yy}(\mathbf{G}) - \sigma_{xx}(\mathbf{G})] (K_x + G_x)(K_y + G_y) \} \\ &\quad \times \frac{J_2(|\mathbf{K} + \mathbf{G}| R_1^A)}{|\mathbf{K} + \mathbf{G}|^2} e^{-i\omega_{\mathbf{K}}t}, \end{aligned} \quad (\text{A6b})$$

where $i = x/y/z$ and $J_n(z)$ is Bessel’s function of the first kind of order n . The integrals are evaluated with the help of the identities

$$\int_0^{2\pi} \cos(m\phi) \exp[i\alpha \cos(\phi - \phi_0)] d\phi = 2\pi i^m J_m(\alpha) \cos \phi_0, \quad (\text{A7a})$$

$$\int_0^{2\pi} \sin(m\phi) \exp[i\alpha \cos(\phi - \phi_0)] d\phi = 2\pi i^m J_m(\alpha) \sin \phi_0, \quad (\text{A7b})$$

where m is an integer, and $\alpha \geq 0$ and ϕ_0 are real numbers. These identities follow from the Jacobi-Anger expansion, in which a plane wave is expressed into a series of cylindrical waves [30]:

$$\exp(iz \cos \phi) = \sum_{n=-\infty}^{+\infty} i^n J_n(z) e^{in\phi}. \quad (\text{A8})$$

Under the rigidity assumption, the (angular) displacement of the cylinder is uniform throughout the object. In what follows, we use the notation introduced in example A in the main text. The linear displacement is taken to be the value at the center of the cylinder, whereas the angular displacement

is determined by averaging over the circumference of the cylinder:

$$X_s^A = u_x(\mathbf{x} = \mathbf{0})e^{-i\omega\mathbf{K}t} = \sum_{\mathbf{G}} u_{x,\mathbf{K}}(\mathbf{G})e^{-i\omega\mathbf{K}t}, \quad (\text{A9a})$$

$$Y_s^A = u_y(\mathbf{x} = \mathbf{0})e^{-i\omega\mathbf{K}t} = \sum_{\mathbf{G}} u_{y,\mathbf{K}}(\mathbf{G})e^{-i\omega\mathbf{K}t}, \quad (\text{A9b})$$

$$Z_s^A = u_z(\mathbf{x} = \mathbf{0})e^{-i\omega\mathbf{K}t} = \sum_{\mathbf{G}} u_{z,\mathbf{K}}(\mathbf{G})e^{-i\omega\mathbf{K}t}, \quad (\text{A9c})$$

$$\begin{aligned} \Psi_s^A &= \frac{1}{2\pi R_1^A} \oint_{|s=R_1^A} dl \frac{1}{R_1^A} (-u_x \sin \phi + u_y \cos \phi) \\ &= \frac{i}{R_1^A} \sum_{\mathbf{G}} [-u_{x,\mathbf{K}}(\mathbf{G})(K_y + G_y) + u_{y,\mathbf{K}}(\mathbf{G})(K_x + G_x)] \\ &\quad \times \frac{J_1(|\mathbf{K} + \mathbf{G}|R_1^A)}{|\mathbf{K} + \mathbf{G}|} e^{-i\omega\mathbf{K}t}. \end{aligned} \quad (\text{A9d})$$

The spring tensor is defined as the elastic force per unit displacement. The out-of-plane spring tensor element $k_{b,zz}$ is evaluated using Eqs. (A6a) and (A9c):

$$k_{b,zz}(\mathbf{K}) = -\frac{F_{b,z}(\mathbf{K})}{Z_s^A}. \quad (\text{A10})$$

The first three in-plane acoustic bands are predominated by the coupled in-plane translation and rotation of the rigid cylinders. The in-plane spring tensor components are then calculated using Eqs. (A6a), (A6b), (A9a), (A9b), and (A9d):

$$\begin{aligned} &\begin{pmatrix} k_{b,xx}(\mathbf{K}) & k_{b,xy}(\mathbf{K}) & k_{b,x\psi}(\mathbf{K}) \\ k_{b,yx}(\mathbf{K}) & k_{b,yy}(\mathbf{K}) & k_{b,y\psi}(\mathbf{K}) \\ k_{b,\psi x}(\mathbf{K}) & k_{b,\psi y}(\mathbf{K}) & k_{b,\psi\psi}(\mathbf{K}) \end{pmatrix} \\ &= -\begin{pmatrix} F_{b,x}^{(1)} & F_{b,x}^{(2)} & F_{b,x}^{(3)} \\ F_{b,y}^{(1)} & F_{b,y}^{(2)} & F_{b,y}^{(3)} \\ \tau_{b,\psi}^{(1)} & \tau_{b,\psi}^{(2)} & \tau_{b,\psi}^{(3)} \end{pmatrix} \begin{pmatrix} X_s^{(1)} & X_s^{(2)} & X_s^{(3)} \\ Y_s^{(1)} & Y_s^{(2)} & Y_s^{(3)} \\ \Psi_s^{(1)} & \Psi_s^{(2)} & \Psi_s^{(3)} \end{pmatrix}^{-1}. \end{aligned} \quad (\text{A11})$$

Accordingly, we introduce the band index superscripts $j = 1, 2, 3$ to select the associated dispersion relation $\omega_{\mathbf{K}}^{(j)}$. The displacement and forces are likewise labeled with the corresponding superscripts.

APPENDIX B: BACKGROUND SPRING TENSOR BY MULTIPLE SCATTERING OF PARTIAL WAVES

The method of multiple scattering derives from the periodic superposition of the single-scatterer wave functions and the boundary conditions on the scatterers' surface. It is more generally known as the Korringa–Kohn–Rostoker method (KKR method) [31–33] in the context of the electronic band structure calculations involving the quantum mechanical wave function of electrons in periodic solids. In this Appendix, the spring tensor is evaluated using multiple scattering of cylindrical partial waves.

The underlying matrices in cylindrical wave basis are theoretically infinite in size. They are truncated with 21 cylindrical waves ($-10 \leq l \leq 10$). The results are in substantial agreement with the calculations by plane-wave expansion presented in Appendix C and in Figs. 2, 3(a), and 3(b) of the main text.

The out-of-plane displacement u_z satisfies the wave equation (5). In a unit cell (see Fig. 1), the general solution in cylindrical coordinates is given by

$$u_z(s, \phi) = \begin{cases} \sum_{l=-\infty}^{\infty} [A_l J_l(\beta_b s) + B_l Y_l(\beta_b s)] e^{il\phi}, & \text{if } s > R_1^A \\ \sum_{l=-\infty}^{\infty} C_l J_l(\beta_s s) e^{il\phi}, & \text{if } s < R_1^A. \end{cases} \quad (\text{B1})$$

Here, J_l and Y_l are Bessel functions of the first and second kinds of degree l , respectively. $\beta_b = \omega\sqrt{\rho_b/\mu_b}$ and $\beta_s = \omega\sqrt{\rho_s/\mu_s}$ are the wave vectors of the transverse wave in the foam background and the cellulose scatterer, respectively. (λ_b, μ_b) and (λ_s, μ_s) denote the Lamé parameters of the foam background and the cellulose scatterer, respectively. A_l , B_l , and C_l are constants determined by the boundary conditions.

Graf's addition formula allows expansion of an off-center Bessel function into a series of Bessel functions at the coordinate center [30]. Conceptually, one of the scatterers is chosen as the coordinate center, and the cylindrical wave due to a neighboring scatterer centered at a lattice point \mathbf{R} is expressed in the basis of the chosen coordinate origin [30]:

$$\begin{aligned} &Y_l(\beta|\mathbf{r} - \mathbf{R}|) e^{il\phi_{\mathbf{r}-\mathbf{R}}} \\ &= \sum_{m=-\infty}^{\infty} Y_{l+m}(\beta|\mathbf{R}|) J_m(\beta|\mathbf{r}|) e^{im(\phi_{\mathbf{R}} - \phi_{\mathbf{r}})} e^{il(\pi + \phi_{\mathbf{R}})}. \end{aligned} \quad (\text{B2})$$

Here, $\phi_{\mathbf{v}}$ denotes the azimuthal angle of a general vector \mathbf{v} . The addition theorem (B2) is valid for $|\mathbf{r}| < |\mathbf{R}|$, which is always satisfied in our square-lattice structure, when the domain is restricted to the unit cell containing the coordinate center. Together with the discrete translational symmetry of the lattice, one can show that the constants A_l and B_l satisfy the Rayleigh identity [34,35]

$$A_l = \sum_{m=-\infty}^{\infty} (-1)^{l+m} S_{l-m}^Y(\beta_b, \mathbf{K}) B_m, \quad (\text{B3})$$

where $S_l^Y(\beta, \mathbf{K})$ is a lattice sum defined by

$$S_l^Y(\beta, \mathbf{K}) = \sum_{\mathbf{R} \neq \mathbf{0}} Y_l(\beta|\mathbf{R}|) \exp(i\mathbf{K} \cdot \mathbf{R} + il\phi_{\mathbf{R}}). \quad (\text{B4})$$

The lattice sum (B4) is conditionally convergent, and direct computation is often impractical. By relating the representations of the cylindrical wave Green's function in position space and reciprocal space, Chin *et al.* [36] reexpressed the lattice sum in reciprocal space as an absolutely convergent series:

$$\begin{aligned} &S_l^Y(\beta, \mathbf{K}) J_{l+1}(\beta a) \\ &= -\left[Y_l(\beta a) + \frac{2}{\pi \beta a} \right] \delta_{l,0} \\ &\quad - \frac{4i^l \beta}{a^2} \sum_{\mathbf{G}} \frac{J_{l+1}(|\mathbf{K} + \mathbf{G}|a)}{|\mathbf{K} + \mathbf{G}|(|\mathbf{K} + \mathbf{G}|^2 - \beta^2)} \exp(il\phi_{\mathbf{K}+\mathbf{G}}). \end{aligned} \quad (\text{B5})$$

On the surface of the cylindrical cellulose scatterer, the out-of-plane displacement u_z and the normal stress $\sigma_{sz} = \mu \partial u_z / \partial s$

are continuous, which relates the constants A_l , B_l , and C_l :

$$A_l J_l(\beta_b R_1^A) + B_l Y_l(\beta_b R_1^A) = C_l J_l(\beta_s R_1^A), \quad (\text{B6a})$$

$$\mu_b [A_l J_l'(\beta_b R_1^A) + B_l Y_l'(\beta_b R_1^A)] = \mu_s [C_l J_l'(\beta_s R_1^A)]. \quad (\text{B6b})$$

The linear system is solved to yield the scattering coefficient M_l :

$$M_l \equiv \frac{A_l}{B_l} = -\frac{\mu_s Y_l(\beta_b R_1^A) J_l'(\beta_s R_1^A) - \mu_b Y_l'(\beta_b R_1^A) J_l(\beta_s R_1^A)}{\mu_s J_l(\beta_b R_1^A) J_l'(\beta_s R_1^A) - \mu_b J_l'(\beta_b R_1^A) J_l(\beta_s R_1^A)}. \quad (\text{B7})$$

Equations (B3) and (B7) yield an eigenvalue equation [34,35]

$$\sum_{m=-\infty}^{\infty} [M_l \delta_{l,m} - (-1)^{l+m} S_{l-m}^Y(\beta_b, \mathbf{K})] B_m = 0. \quad (\text{B8})$$

The nontrivial solution with the lowest eigenfrequency is associated with the out-of-plane translational oscillation of the cellulose shell. This is used to calculate the associated background spring tensor component $k_{b,zz}(\mathbf{K})$:

$$\begin{aligned} k_{b,zz}(\mathbf{K}) &= -\frac{1}{Z_c^A} \int_{\{s=R_1^A\}} \sigma_{zs} dl \\ &= \frac{2\pi R_s^A \mu \beta_b}{Z_c^A} \sum_{l=-\infty}^{\infty} [Y_l(\beta_b R_1^A) \delta_{l,0} \\ &\quad + (-1)^l S_l^Y(\beta_b, \mathbf{K}) J_l(\beta_b R_1^A)] B_l, \end{aligned} \quad (\text{B9})$$

where the out-of-plane oscillation amplitude Z_c^A is approximated by the monopole term ($l=0$) on the surface of the scatterer:

$$Z_c^A = \sum_{l=-\infty}^{\infty} [Y_0(\beta_b R_1^A) \delta_{l,0} + (-1)^l S_l^Y(\beta_b, \mathbf{K}) J_0(\beta_b R_1^A)] B_l. \quad (\text{B10})$$

In an isotropic, linear elastic solid, the in-plane displacement field $u_s \hat{s} + u_\phi \hat{\phi}$ can be reexpressed using in compressional Φ_c and shear Φ_s potentials [18,23,35,37]:

$$u_s = \frac{\partial \Phi_c}{\partial s} + \frac{1}{s} \frac{\partial \Phi_s}{\partial \phi}, \quad (\text{B11a})$$

$$u_\phi = \frac{1}{s} \frac{\partial \Phi_c}{\partial \phi} - \frac{\partial \Phi_s}{\partial s}. \quad (\text{B11b})$$

While the in-plane displacement field components are intricately coupled, the potentials are decoupled and satisfy the wave equations

$$\nabla^2 \Phi_c + \alpha^2 \Phi_c = 0, \quad (\text{B12a})$$

$$\nabla^2 \Phi_s + \beta^2 \Phi_s = 0, \quad (\text{B12b})$$

where $\alpha^2 = \rho \omega^2 / (\lambda + 2\mu)$ and $\beta^2 = \rho \omega^2 / \mu$. In a unit cell, the general solution in cylindrical coordinates is given by

$$\Phi_c(s, \phi) = \begin{cases} \sum_{l=-\infty}^{\infty} [A_l^c J_l(\alpha_b s) + B_l^c Y_l(\alpha_b s)] e^{il\phi}, & \text{if } s > R_1^A \\ \sum_{l=-\infty}^{\infty} C_l^c J_l(\alpha_s s) e^{il\phi}, & \text{if } s < R_1^A \end{cases} \quad (\text{B13a})$$

$$\Phi_s(s, \phi) = \begin{cases} \sum_{l=-\infty}^{\infty} [A_l^s J_l(\beta_b s) + B_l^s Y_l(\beta_b s)] e^{il\phi}, & \text{if } s > R_1^A \\ \sum_{l=-\infty}^{\infty} C_l^s J_l(\beta_s s) e^{il\phi}, & \text{if } s < R_1^A. \end{cases} \quad (\text{B13b})$$

Here, $\alpha_b = \omega \sqrt{\rho_b / (\lambda_b + 2\mu_b)}$ ($\beta_b = \omega \sqrt{\rho_b / \mu_b}$) and $\alpha_s = \omega \sqrt{\rho_s / (\lambda_s + 2\mu_s)}$ ($\beta_s = \omega \sqrt{\rho_s / \mu_s}$) are the wave vectors of the compressional (shear) wave in the foam background and the cellulose scatterer, respectively. A_l^c , B_l^c , C_l^c , A_l^s , B_l^s , and C_l^s are constants determined by the boundary conditions. Using Graf's addition theorem and discrete translational symmetry of the lattice, it can be shown that the constants A_l^c , B_l^c , A_l^s , and B_l^s satisfy the Rayleigh identity [34,35]

$$A_l^c = \sum_{m=-\infty}^{\infty} (-1)^{l+m} S_{l-m}^Y(\alpha_b, \mathbf{K}) B_m^c, \quad (\text{B14a})$$

$$A_l^s = \sum_{m=-\infty}^{\infty} (-1)^{l+m} S_{l-m}^Y(\beta_b, \mathbf{K}) B_m^s. \quad (\text{B14b})$$

On the surface of the cylindrical scatterer, the in-plane displacement field components u_s and u_ϕ and the normal

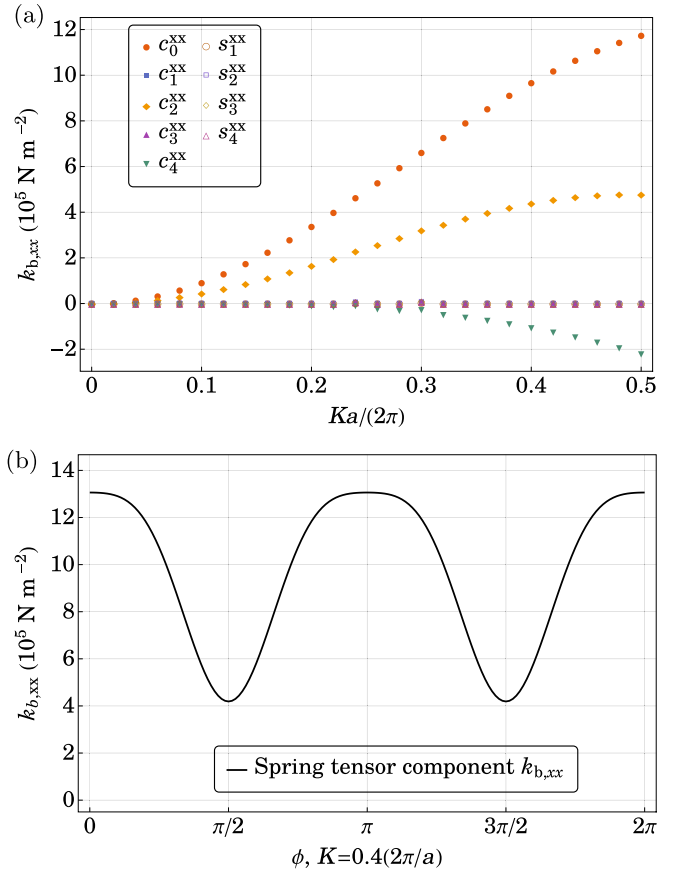


FIG. 18. Dependence of $k_{b,xx}$ on the magnitude and orientation of the Bloch wave vector \mathbf{K} . (a) The diagonal spring tensor component $k_{b,xx}$ describes the force per unit length acting on the cylindrical shell in the x direction, per unit displacement in the same direction. Its Fourier coefficients (up to the fourth harmonics) are plotted from the center of the first Brillouin zone to the radius of the largest inscribed circle at $K = 0.5(2\pi/a)$. (b) The spring tensor component $k_{b,xx}$ is plotted as a function of the orientation ϕ of the wave vector at a fixed magnitude $K = 0.4(2\pi/a)$. The angular dependence of $k_{b,xx}$ is predominated by the zeroth, second, and fourth harmonics, in the order of decreasing significance. The diagonal element has nonzero angular average.

stress components σ_{ss} and $\sigma_{\phi s}$ are continuous. In terms of the compressional and shear waves, the relevant normal stress components are given by

$$\sigma_{ss} = 2\mu \left[-\frac{1}{s} \frac{\partial \Phi_c}{\partial s} - \frac{1}{s^2} \frac{\partial^2 \Phi_c}{\partial \phi^2} + \frac{1}{s} \frac{\partial^2 \Phi_s}{\partial s \partial \phi} - \frac{1}{s^2} \frac{\partial \Phi_s}{\partial \phi} \right] - \rho \omega^2 \Phi_c, \quad (\text{B15a})$$

$$\sigma_{\phi s} = 2\mu \left[\frac{1}{s} \frac{\partial^2 \Phi_c}{\partial s \partial \phi} - \frac{1}{s^2} \frac{\partial \Phi_c}{\partial \phi} + \frac{1}{s} \frac{\partial \Phi_s}{\partial s} + \frac{1}{s^2} \frac{\partial^2 \Phi_s}{\partial \phi^2} \right] + \rho \omega^2 \Phi_s. \quad (\text{B15b})$$

Continuity of the expressions (B11a), (B11b), (B15a), and (B15b) across material boundary are solved to yield a set of

scattering coefficients $\{M_l^{cc}, M_l^{cs}, M_l^{sc}, M_l^{ss}\}$, relating the constants $A_l^c, A_l^s, B_l^c,$ and B_l^s :

$$A_l^c = M_l^{cc} B_l^c + M_l^{cs} B_l^s, \quad (\text{B16a})$$

$$A_l^s = M_l^{sc} B_l^c + M_l^{ss} B_l^s. \quad (\text{B16b})$$

Explicit expressions of the scattering coefficients can be found in Appendix C of [37] and Appendix B of [38]. Readers should exercise caution when adopting multiple scattering schemes from the literature [34,37–40], as there are different sign conventions in the definitions of the lattice sum and scattering coefficients. Equations (B14a), (B14b), (B16a), and

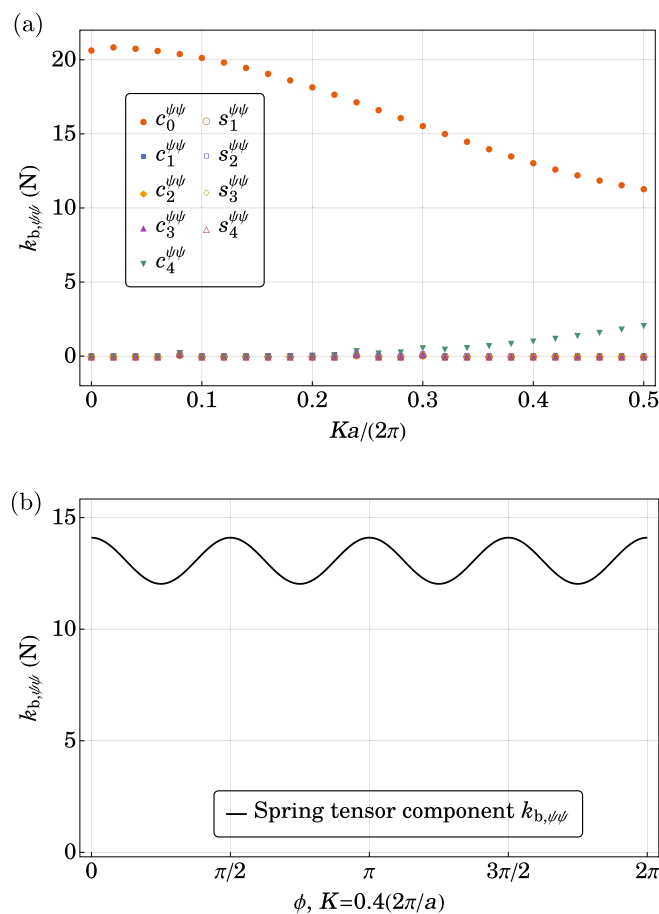


FIG. 19. Dependence of $k_{b,\psi\psi}$ on the magnitude and orientation of the Bloch wave vector \mathbf{K} . (a) The diagonal spring tensor component $k_{b,\psi\psi}$ describes the torque per unit length acting on the cylindrical shell in the ψ direction, per unit angular displacement in the same direction. Its Fourier coefficients (up to the fourth harmonics) are plotted from the center of the first Brillouin zone to the radius of the largest inscribed circle at $K = 0.5(2\pi/a)$. (b) The spring tensor component $k_{b,\psi\psi}$ is plotted as a function of the orientation ϕ of the wave vector at a fixed magnitude $K = 0.4(2\pi/a)$. The angular dependence of $k_{b,\psi\psi}$ is predominated by the zeroth and the fourth harmonics, in the order of decreasing significance. The diagonal element has nonzero angular average.

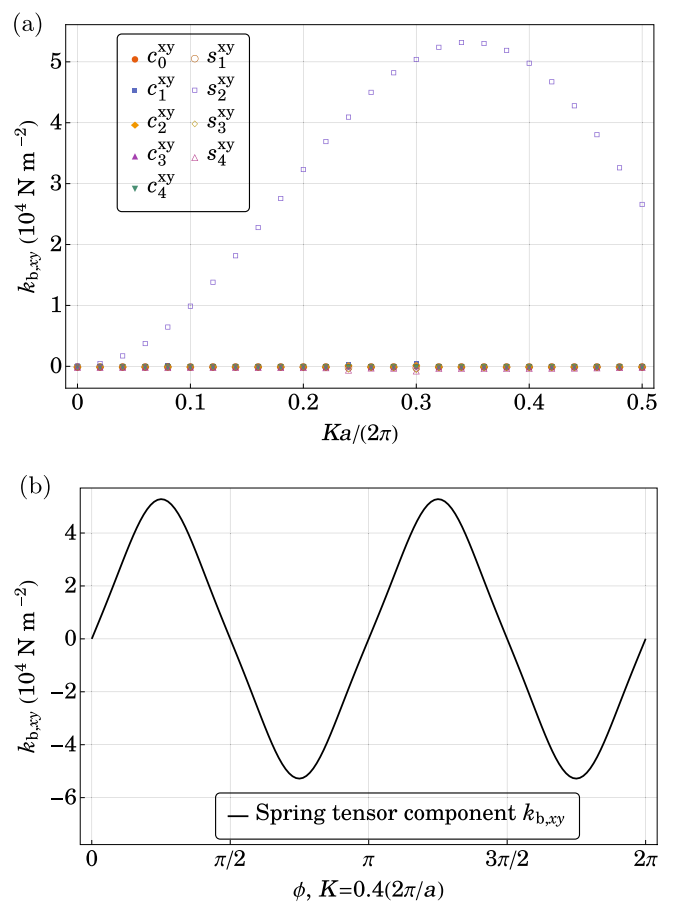


FIG. 20. Dependence of $k_{b,xy}$ on the magnitude and orientation of the Bloch wave vector \mathbf{K} . (a) The off-diagonal spring tensor component $k_{b,xy}$ describes the force per unit length acting on the cylindrical shell in the x direction, per unit displacement in the y direction. Its Fourier coefficients (up to the fourth harmonics) are plotted from the center of the first Brillouin zone to the radius of the largest inscribed circle at $K = 0.5(2\pi/a)$. (b) The spring tensor component $k_{b,xy}$ is plotted as a function of the orientation ϕ of the wave vector at a fixed magnitude $K = 0.4(2\pi/a)$. The angular dependence of $k_{b,xy}$ is predominated by the second harmonics. The off-diagonal component has zero angular average. The next nonvanishing harmonics is the sixth harmonics (not shown in graph).

(B16b) yield a matrix eigenvalue equation, governing the in-plane eigenmodes [35,37]

$$\sum_{m=-\infty}^{\infty} (M_m^{cc} B_m^c + M_m^{cs} B_m^s) \delta_{lm} - (-1)^{l+m} S_{l-m}^Y(\alpha_b, \mathbf{K}) B_m^c = 0, \quad (\text{B17a})$$

$$\sum_{m=-\infty}^{\infty} (M_m^{sc} B_m^c + M_m^{ss} B_m^s) \delta_{lm} - (-1)^{l+m} S_{l-m}^Y(\beta_b, \mathbf{K}) B_m^s = 0. \quad (\text{B17b})$$

The in-plane angular displacement Ψ_s^A of the cellulose cylinder is given by the monopole term ($l=0$) of the shear wave, whereas the in-plane linear displacement $X_s^A \hat{\mathbf{x}} + Y_s^A \hat{\mathbf{y}}$ arises from the dipole terms ($l=\pm 1$) of the compressional and shear waves: $\mathbf{u}(s=R_1^A) = u_s(s=R_1^A) \hat{\mathbf{s}} + u_\phi(s=R_1^A) \hat{\boldsymbol{\phi}} = (X_s^A \cos \phi + Y_s^A \sin \phi) \hat{\mathbf{s}} + (R_s^A \Psi_s^A - X_s^A \sin \phi + Y_s^A \cos \phi) \hat{\boldsymbol{\phi}}$. Using Eqs. (B11a) and (B11b), the (angular) displacements are expressed in terms of the radial derivatives and angular harmonics of the elastic potentials:

$$\begin{aligned} X_s^A &= \Phi'_{c,1} + \Phi'_{c,-1} + \frac{i}{R_1^A} (\Phi_{s,1} - \Phi_{s,-1}) \\ &= \frac{1}{R_1^A} (\Phi_{c,1} + \Phi_{c,-1}) + i(\Phi'_{s,1} - \Phi'_{s,-1}), \end{aligned} \quad (\text{B18a})$$

$$\begin{aligned} Y_s^A &= i(\Phi'_{c,1} - \Phi'_{c,-1}) - \frac{1}{R_1^A} (\Phi_{s,1} + \Phi_{s,-1}) \\ &= \frac{i}{R_1^A} (\Phi_{c,1} - \Phi_{c,-1}) - (\Phi'_{s,1} + \Phi'_{s,-1}), \end{aligned} \quad (\text{B18b})$$

$$\Psi_s^A = -\frac{1}{R_1^A} \Phi'_{s,0}. \quad (\text{B18c})$$

The force $F_{b,x} \hat{\mathbf{x}} + F_{b,y} \hat{\mathbf{y}}$ and axial torque $\tau_{b,\psi} \hat{\mathbf{z}}$ per unit length in the axial direction, acting on the cellulose scatterer by the background foam, are given by

$$\begin{aligned} F_{b,x} &= \oint_{\{s=R_1^A\}} (\sigma_{ss} \cos \phi - \sigma_{\phi s} \sin \phi) dl \\ &= \pi R_1^A \rho_b \omega^2 (-\Phi_{c,1} - \Phi_{c,-1} - i\Phi_{s,1} + i\Phi_{s,-1}), \end{aligned} \quad (\text{B19a})$$

$$\begin{aligned} F_{b,y} &= \oint_{\{s=R_1^A\}} (\sigma_{ss} \sin \phi + \sigma_{\phi s} \cos \phi) dl \\ &= \pi R_1^A \rho_b \omega^2 (-i\Phi_{c,1} + i\Phi_{c,-1} + \Phi_{s,1} + \Phi_{s,-1}), \end{aligned} \quad (\text{B19b})$$

$$\tau_{b,\psi} = \oint_{\{s=R_1^A\}} s \sigma_{\phi s} dl = 4\pi \mu_b R_1^A \Phi'_{s,0} + 2\pi \rho_b \omega^2 (R_1^A)^2 \Phi_{s,0}. \quad (\text{B19c})$$

Here, $\Phi_{c,l}$ and $\Phi_{s,l}$ denote the coefficient of $e^{il\phi}$ of $\Phi_c(R_1^A, \phi)$ and $\Phi_s(R_1^A, \phi)$ in Eqs. (B13a) and (B13b), respectively. The ‘‘prime’’ superscript denotes spatial derivative with respect to the radial variable s :

$$\Phi_{c,l} = \sum_{m=-\infty}^{\infty} [Y_l(\alpha_b R_1^A) \delta_{lm} + (-1)^{l+m} S_{l-m}^Y(\alpha_b, \mathbf{K}) J_l(\alpha_b R_1^A)] B_m^c, \quad (\text{B20a})$$

$$\Phi'_{c,l} = \frac{\alpha_b}{2} \sum_{m=-\infty}^{\infty} \{ [Y_{l-1}(\alpha_b R_1^A) - Y_{l+1}(\alpha_b R_1^A)] \delta_{lm} + (-1)^{l+m} S_{l-m}^Y(\alpha_b, \mathbf{K}) [J_{l-1}(\alpha_b R_1^A) - J_{l+1}(\alpha_b R_1^A)] \} B_m^c, \quad (\text{B20b})$$

$$\Phi_{s,l} = \sum_{m=-\infty}^{\infty} [Y_l(\beta_b R_1^A) \delta_{lm} + (-1)^{l+m} S_{l-m}^Y(\beta_b, \mathbf{K}) J_l(\beta_b R_1^A)] B_m^s, \quad (\text{B20c})$$

$$\Phi'_{s,l} = \frac{\beta_b}{2} \sum_{m=-\infty}^{\infty} \{ [Y_{l-1}(\beta_b R_1^A) - Y_{l+1}(\beta_b R_1^A)] \delta_{lm} + (-1)^{l+m} S_{l-m}^Y(\beta_b, \mathbf{K}) [J_{l-1}(\beta_b R_1^A) - J_{l+1}(\beta_b R_1^A)] \} B_m^s. \quad (\text{B20d})$$

These expressions are obtained using the Rayleigh identities (B14a) and (B14b), and the identities $J'_l(z) = (\frac{1}{2})[J_{l-1}(z) - J_{l+1}(z)]$ and $Y'_l(z) = (\frac{1}{2})[Y_{l-1}(z) - Y_{l+1}(z)]$. The spring tensor components are then calculated from the knowledge of first three in-plane acoustic bands, using the expression (A11) in Appendix A and the results of Eqs. (B18a), (B18b), (B18c), (B19a), (B19b), and (B19c).

The formulation in partial cylindrical waves provides further justification of our EIST model. We show that in the limit when the shell is orders of magnitude more rigid than the background foam $\mu_s \gg \mu_b$, only the monopole response contributes to the lowest-frequency out-of-plane eigenmode and the oscillation of the scatterer obeys Newton’s second law. In the rigid shell limit, wavelike deformation in the scatterer is negligible $\beta_s R_1^A \ll 1$ and $J_l(\beta_s R_1^A) \propto (\beta_s R_1^A)^l$. For $l \neq 0$, the terms multiplied by μ_s dominate the terms multiplied

by μ_b , and the scattering coefficient (B7) approaches the s -polarization limit:

$$M_{l \neq 0} \rightarrow -\frac{Y_l(\beta_b R_1^A)}{J_l(\beta_b R_1^A)}, \quad (\text{B21})$$

$$C_{l \neq 0} = \left(M_l + \frac{Y_l(\beta_b R_1^A)}{J_l(\beta_b R_1^A)} \right) B_l \rightarrow 0. \quad (\text{B22})$$

This reveals that the multipolar deformation of the shell is negligible in the rigid shell limit. It should be noted that the monopolar term M_0 does not approach the same limit because of the cancellation $\mu_s J'_0(\beta_s R_s^A) \approx (-\frac{1}{2}) \mu_s \beta_s^2 R_s^A = (-\frac{1}{2}) \rho_s \omega^2 R_s^A$. As such, the continuity conditions of the

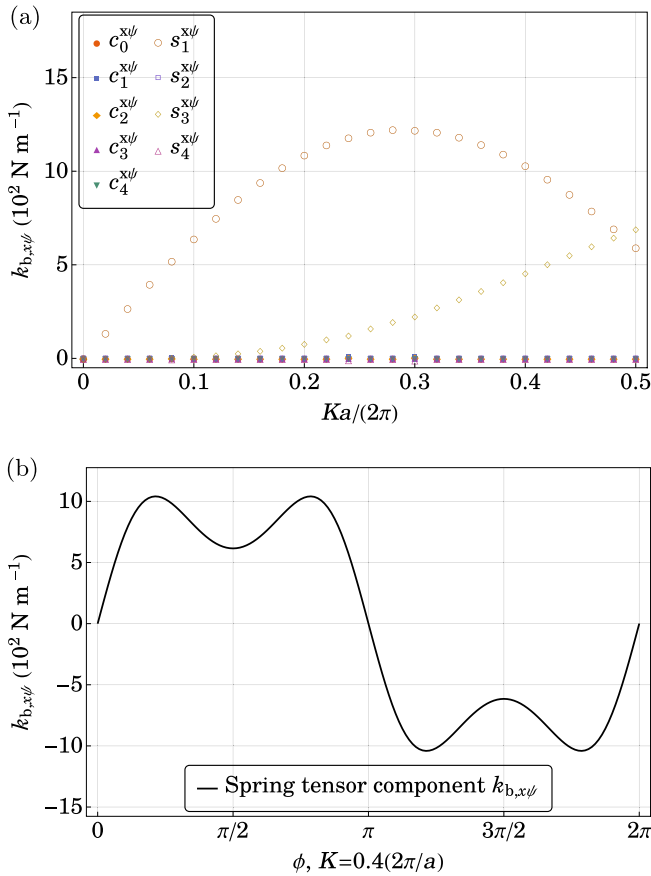


FIG. 21. Dependence of $k_{b,x\psi}$ on the magnitude and orientation of the Bloch wave vector \mathbf{K} . (a) The off-diagonal spring tensor component $k_{b,x\psi}$ describes the force per unit length acting on the cylindrical shell in the x direction, per unit angular displacement in the ψ direction. Its Fourier coefficients (up to the fourth harmonics) are plotted from the center of the first Brillouin zone to the radius of the largest inscribed circle at $K = 0.5(2\pi/a)$. (b) The spring tensor component $k_{b,x\psi}$ is plotted as a function of the orientation ϕ of the wave vector at a fixed magnitude $K = 0.4(2\pi/a)$. The angular dependence of $k_{b,x\psi}$ is predominated by the first and the third harmonics, in the order of decreasing significance. The off-diagonal component has zero angular average. The next nonvanishing harmonics is the fifth harmonics (not shown in graph).

displacement (B6a) and normal stress (B6b) simplify to

$$A_0 J_0(\beta_b R_1^A) + B_0 Y_0(\beta_b R_1^A) = C_0, \quad (\text{B23a})$$

$$\mu_b [A_0 J_0'(\beta_b R_1^A) + B_0 Y_0'(\beta_b R_1^A)] = -\frac{1}{2} C_0 \rho_s \omega^2 R_1^A. \quad (\text{B23b})$$

We identify the monopolar response C_0 as the out-of-plane oscillation amplitude $C_0 = Z_s^A$. Equation (B23a) is an equivalent expression of the $l = 0$ rigid shell approximation in (B10). Equation (B23b) is identified as the Newton's second law of the rigid cellulose shell:

$$-\rho_s \pi (R_1^A)^2 \omega^2 Z_s^A = 2\pi R_1^A \mu_b [A_0 J_0'(\beta_b R_1^A) + B_0 Y_0'(\beta_b R_1^A)], \quad (\text{B24})$$

where the force term on the right-hand side is identical to the restoring force $-k_{b,zz} Z_s^A$ in Eq. (B9), using $J_0'(x) = -J_1(x)$, $Y_0'(x) = -Y_1(x)$, and the Rayleigh identity (B3). In models B and C, the nonresonant scatterers in model A are replaced by resonant scatterers occupying the same volume. If the outermost shell is orders of magnitude stiffer than the background medium, the multipolar terms are negligible and the rigid shell has a well-defined out-of-plane displacement associated with the monopolar term. The background medium obeys the same boundary conditions, and the same background spring tensor applies.

APPENDIX C: SYMMETRIES AND WAVE-VECTOR DEPENDENCE OF THE SPRING TENSOR

The dependence of the spring tensor components $k_{b,xx}(\mathbf{K})$, $k_{b,\psi\psi}(\mathbf{K})$, $k_{b,xy}(\mathbf{K})$, and $k_{b,x\psi}(\mathbf{K})$ on the magnitude K and the orientation ϕ of the wave vector \mathbf{K} are plotted in Figs. 18, 19, 20, and 21, respectively. All the diagonal components have nonzero angular averages, while all the off-diagonal components have zero angular averages.

The other five components are related to the four explicitly plotted components by symmetry. The spring tensor is symmetric, so that $k_{b,xy}(\mathbf{K}) = k_{b,yx}(\mathbf{K})$, $k_{b,x\psi}(\mathbf{K}) = k_{b,\psi x}(\mathbf{K})$, $k_{b,y\psi}(\mathbf{K}) = k_{b,\psi y}(\mathbf{K})$. Lattice symmetry heavily constrains the dependence of the spring tensor on direction of the wave vector. Because of the fourfold discrete rotational symmetry of the lattice, the only nonvanishing Fourier components of $k_{b,zz}$ and $k_{b,\psi\psi}$ are the $4n$ th harmonics. The discrete rotational symmetry of square lattice also implies that $k_{b,yy}(K, \phi) = k_{b,xx}(K, \phi - \pi/2)$ and $k_{b,y\psi}(K, \phi) = k_{b,x\psi}(K, \phi - \pi/2)$.

[1] M. S. Kushwaha, P. Halevi, L. Dobrzynski, and B. Djafari-Rouhani, *Phys. Rev. Lett.* **71**, 2022 (1993).
 [2] F. R. Montero de Espinosa, E. Jiménez, and M. Torres, *Phys. Rev. Lett.* **80**, 1208 (1998).
 [3] J. V. Sánchez-Pérez, D. Caballero, R. Martínez-Sala, C. Rubio, J. Sánchez-Dehesa, F. Meseguer, J. Linares, and F. Gálvez, *Phys. Rev. Lett.* **80**, 5325 (1998).
 [4] J. O. Vasseur, P. A. Deymier, B. Chenni, B. Djafari-Rouhani, L. Dobrzynski, and D. Prevost, *Phys. Rev. Lett.* **86**, 3012 (2001).
 [5] Z. Liu, X. Zhang, Y. Mao, Y. Y. Zhu, Z. Yang, C. T. Chan, and P. Sheng, *Science* **289**, 1734 (2000).

[6] Z. Liu, C. T. Chan, and P. Sheng, *Phys. Rev. B* **65**, 165116 (2002).
 [7] A. Colombi, P. Roux, S. Guenneau, and M. Rupin, *J. Acoust. Soc. Am.* **137**, 1783 (2015).
 [8] M. Dubois, E. Bossy, S. Enoch, S. Guenneau, G. Lerosey, and P. Sebbah, *Phys. Rev. Lett.* **114**, 013902 (2015).
 [9] K. L. S. Yip and S. John, *Phys. Rev. B* **103**, 094304 (2021).
 [10] O. Toader and S. John, *Phys. Rev. E* **70**, 046605 (2004).
 [11] G. Ma and P. Sheng, *Sci. Adv.* **2**, e1501595 (2016).
 [12] D. Torrent and J. Sánchez-Dehesa, *New J. Phys.* **13**, 093018 (2011).

- [13] S. Nemat-Nasser, J. R. Willis, A. Srivastava, and A. V. Amirkhizi, *Phys. Rev. B* **83**, 104103 (2011).
- [14] A. N. Norris, A. L. Shuvalov, and A. A. Kutsenko, *Proc. R. Soc. London A* **468**, 1629 (2012).
- [15] D. Torrent, Y. Pennec, and B. Djafari-Rouhani, *Phys. Rev. B* **92**, 174110 (2015).
- [16] J. Li and C. T. Chan, *Phys. Rev. E* **70**, 055602(R) (2004).
- [17] Y. Wu, Y. Lai, and Z.-Q. Zhang, *Phys. Rev. B* **76**, 205313 (2007).
- [18] L. Landau, E. Lifshitz, A. Kosevich, J. Sykes, L. Pitaevskii, and W. Reid, *Theory of Elasticity: Volume 7*, Course of Theoretical Physics (Elsevier, Oxford, 1986).
- [19] M. S. Kushwaha, P. Halevi, G. Martínez, L. Dobrzynski, and B. Djafari-Rouhani, *Phys. Rev. B* **49**, 2313 (1994).
- [20] H. M. Ledbetter, N. V. Frederick, and M. W. Austin, *J. Appl. Phys.* **51**, 305 (1980).
- [21] J. Carvill, *Mechanical Engineer's Data Handbook* (Butterworth Heinemann, Oxford, 1993).
- [22] B. Moore, T. Jaglinski, D. Stone, and R. Lakes, *Cell. Polym.* **26**, 1 (2007).
- [23] Z. Liu, C. T. Chan, and P. Sheng, *Phys. Rev. B* **71**, 014103 (2005).
- [24] Z. Yang, J. Mei, M. Yang, N. H. Chan, and P. Sheng, *Phys. Rev. Lett.* **101**, 204301 (2008).
- [25] A. Chutinan and S. John, *Phys. Rev. A* **78**, 023825 (2008).
- [26] S. Bhattacharya and S. John, *APL Photonics* **5**, 020902 (2020).
- [27] L. Li, *J. Opt. Soc. Am. A* **13**, 1870 (1996).
- [28] P. Lalanne, *Phys. Rev. B* **58**, 9801 (1998).
- [29] Y. Cao, Z. Hou, and Y. Liu, *Phys. Lett. A* **327**, 247 (2004).
- [30] M. Abramowitz and I. A. Stegun, *Handbook of Mathematical Functions with Formulas, Graphs, and Mathematical Tables*, 10th ed. (Dover, New York, 1964), p. 363.
- [31] J. Kortinga, *Physica (Amsterdam)* **13**, 392 (1947).
- [32] W. Kohn and N. Rostoker, *Phys. Rev.* **94**, 1111 (1954).
- [33] W. Jones and N. March, *Theoretical Solid State Physics*, Dover Books on Physics and Chemistry, Vol. 2 (Dover, New York, 1985).
- [34] N. A. Nicorovici, R. C. McPhedran, and L. C. Botten, *Phys. Rev. E* **52**, 1135 (1995).
- [35] C. G. Poulton, A. B. Movchan, R. C. McPhedran, N. A. Nicorovici, and Y. A. Antipov, *Proc. R. Soc. London A* **456**, 2543 (2000).
- [36] S. K. Chin, N. A. Nicorovici, and R. C. McPhedran, *Phys. Rev. E* **49**, 4590 (1994).
- [37] A. B. Movchan, N. A. Nicorovici, and R. C. McPhedran, *Proc.: Math., Phys. Eng. Sci.* **453**, 643 (1997).
- [38] J. Mei, Z. Liu, J. Shi, and D. Tian, *Phys. Rev. B* **67**, 245107 (2003).
- [39] J. Mei, Z. Liu, and C. Qiu, *J. Phys.: Condens. Matter* **17**, 3735 (2005).
- [40] L. Cai, H. Xiaoyun, and W. Xisen, *Phys. Rev. B* **74**, 153101 (2006).